Available online at www.sciencedirect.com

ScienceDirect

Geochimica et Cosmochimica Acta 207 (2017) 19–42

Geochimica et Cosmochimica Acta

www.elsevier.com/locate/gca

Fluid-induced transition from banded kyanite- to bimineralic eclogite and implications for the evolution of cratons

H. Sommer [a,*], D.E. Jacob [b], R.A. Stern [c], D. Petts [c], D.P. Mattey [d], D.G. Pearson [c]

[a] School of Geography, Earth Science and Environment, The University of the South Pacific, Laucala Campus, Suva, Fiji
[b] Australian Research Council Centre of Excellence for Core to Crust Fluid Systems and Department of Earth and Planetary Science, Macquarie University, North Ryde, Sydney, NSW 2109, Australia
[c] Deptartment of Earth and Atmospheric Sciences, University of Alberta, Edmonton, Alberta T6G 2E3, Canada
[d] Department of Geology, Royal Holloway University of London, Egham, Surrey TW20 OEX, United Kingdom

Received 16 October 2016; accepted in revised form 14 March 2017; Available online 21 March 2017

Abstract

Heterogeneous, modally banded kyanite-bearing and bimineralic eclogites from the lithospheric mantle, collected at the Roberts Victor Diamond mine (South Africa), show a reaction texture in which kyanite is consumed. Geothermobarometric calculations using measured mineral compositions in Perple_X allowed the construction of a *P-T* path showing a steep, cool prograde metamorphic gradient of 2 °C/km to reach peak conditions of 5.8 GPa and 890 °C for the kyanite eclogite. The kyanite-out reaction formed bimineralic eclogite and is probably an integral part of the mineralogical evolution of most archetypal bimineralic eclogites at Roberts Victor and potentially elsewhere. The kyanite-out reaction occured at close to peak pressure (5.3 GPa) and was associated with a rise in temperature to 1380 °C. Mass balance calculations show that upon breakdown, the kyanite component is fully accommodated in garnet and omphacite via a reaction system with low water fugacity that required restricted fluid influx from metasomatic sources. The $\delta^{18}O$ values of garnets are consistently higher than normal mantle values. Each sample has its characteristic trend of $\delta^{18}O$ variance between garnets in the kyanite-bearing sections and those in the bimineralic parts covering a range between 5.1‰ and 6.8‰. No systematic change in O-isotope signature exists across the sample population. Differences in garnet trace element signatures between differing lithologies in the eclogites are significant. Grossular-rich garnets coexisting with kyanite have strong positive Eu-anomalies and low Gd/Yb ratios, while more pyrope-rich garnets in the bimineralic sections have lost their positive Eu-anomaly, have higher Gd/Yb ratios and generally higher heavy rare earth element contents. Garnets in the original kyanite-bearing portions thus reflect the provenance of the rocks as metamorphosed gabbros/troctolites. The kyanite-out reaction was most likely triggered by a heating event in the subcratonic lithosphere. As kyanite contains around 100 ppm of H_2O it is suggested that the kyanite-out reaction, once initiated by heating and restricted metasomatic influx, was promoted by the release of water contained in the kyanite. The steep (high-P low-T) prograde *P-T* path defining rapid compression at low heating rates is atypical for subduction transport of eclogites into the lithospheric mantle. Such a trajectory is best explained in a model where strong lateral compression forces eclogites downward to higher pressures, supporting models of cratonic lithosphere formation by lateral collision and compression.

Keywords: Kaapvaal craton; Cratonic lithosphere; Perple_X; Kyanite; Oxygen isotopes; Eclogite

* Corresponding author.
E-mail addresses: info@holgersommer.de (H. Sommer), dorrit.jacob@mq.edu.au (D.E. Jacob), rstern@ualberta.ca (R.A. Stern), dpetts@uottawa.ca (D. Petts), d.mattey@rhul.ac.uk (D.P. Mattey), gdpearso@ualberta.ca (D.G. Pearson).

http://dx.doi.org/10.1016/j.gca.2017.03.017
0016-7037/

1. INTRODUCTION

Many eclogite xenoliths brought up by kimberlites are subducted oceanic crustal rocks with an often complex history of melting and metasomatic re-enrichment in the mantle (Shervais et al., 1988; Taylor and Neal, 1989; Jacob et al., 1994; Viljoen et al., 1994; Snyder et al., 1997; Barth et al., 2001; Shirey et al., 2001; Usui et al., 2006; Nikitina et al., 2014; Dongre et al., 2015). Some eclogite xenolith suites are interpreted as subducted residues of tonalitic melt removal (Ireland et al., 1994; Rollinson, 1997; Jacob and Foley, 1999; Barth et al., 2002; Rapp et al., 2003; Tappe et al., 2011; Pernet-Fisher et al., 2014; Smit et al., 2014) and more rarely, some are interpreted to represent high-pressure magmatic cumulates (e.g. MacGregor and Carter, 1970; Snyder et al., 1997; Taylor et al., 2003; Greau et al., 2011; Huang et al., 2012). Radiogenic ages of eclogite xenoliths reach well back into the Archaean (Pearson et al., 1995; Jacob and Foley, 1999; Shirey et al., 2001; Tappe et al., 2011; Aulbach and Viljoen, 2015) and are interpreted to represent the age of metamorphism/subduction. These rocks are thus amongst the oldest high-grade metamorphic rocks on Earth and may represent some of the best preserved samples of Archaean oceanic crust.

Most eclogite xenoliths in kimberlites are bimineralic in nature and are likely to have been modified by melt extraction, metasomatism, or both. In contrast, kyanite-bearing eclogites occur in the xenolith suites of a number of kimberlite localities worldwide and probably represent a more pristine sample of the eclogite assemblage judging from the reaction textures observed in some of them (Lappin and Dawson, 1975). At the Roberts Victors Mine on the Kaapvaal craton in South Africa, kyanite eclogites are relatively common where particularly large specimens of kyanite-bearing eclogite have been found, often interlayered with bimineralic lithologies. Kyanite is a prograde metamorphic mineral that forms by the breakdown of plagioclase in gabbroic rocks of the oceanic crust (Shu et al., 2016). Its occurrence in eclogite xenoliths is key evidence of their crustal origin, because the high Al_2O_3 content of kyanite excludes equilibrium with the peridotitic mantle, and high-pressure mantle melts cannot precipitate kyanite (Jacob et al., 1998). In the absence of a fluid or melt to facilitate diffusion and melting (Wayte et al., 1989), kyanite can persist in metastable form at basal lithospheric temperatures and pressures (ca. 1300 °C, 5.5 GPa, Mather et al., 2011). Upon breakdown, the aluminum from kyanite can be accommodated in the extensive solid-solution series of garnet and clinopyroxene. Petrographic evidence for kyanite resorption and breakdown is common in the eclogite xenolith record (e.g. Lappin and Dawson 1975; Dongre et al., 2015). The layered kyanite eclogites from Roberts Victor provide perhaps the most spectacular examples of this process.

This study presents a detailed quantitative geochemical and mass balance study of five large kyanite-bearing eclogites from the Roberts Victor Mine. We show that the kyanite-bearing portions of these composite xenoliths represent relict low-pressure assemblages developed in a prograde *P-T* path, while the associated bimineralic parts are fluid-assisted subsolidus reaction products of a kyanite-out reaction that occurred at mantle pressures and temperatures.

2. THE ROBERTS VICTOR KIMBERLITE AND ITS ECLOGITE SUITE

The Roberts Victor Mine is situated in the Kaapvaal craton, RSA in close vicinity to the Colesberg lineament (Silver et al., 2004). The mine consists of two small pipes that intrude the Beaufort Sandstone and Karoo Basalts (Field et al., 2008). The kimberlite is classified as a mica-rich Group-2 kimberlite and is dated at ~128 Ma using Rb–Sr on phlogopites (Smith et al., 1985). It is extraordinarily rich in mantle xenoliths, especially in eclogites, which make up 80–90% of the fresher xenoliths in this pipe (MacGregor and Carter, 1970). The age of the eclogite xenolith suite is 2700 ± 100 Ma using Sm-Nd (Jagoutz et al., 1984). In contrast to the xenoliths, the heavy mineral concentrate in Roberts Victor is dominated by peridotitic material (Schulze, 1989); the few peridotitic xenoliths found at Roberts Victor are diamondiferous (Viljoen et al., 1994) but highly altered.

A combined textural-compositional classification based of bimineralic eclogites differentiates diamondiferous Group I eclogites as equilibrated at high *P-T* (4.5–7.0 GPa, 980–1550 °C), displaying subhedral garnets with high Na_2O concentration >0.09 wt%, and Group II eclogites, which are non-diamondiferous, equilibrated at lower *P-T* (1.7–4.5 GPa, 730–1100 °C), with interlocking angular mineral fabric and lower Na_2O contents in garnet (MacGregor and Carter, 1970; McCandless and Gurney, 1989). Group I eclogites make up the majority of the suite at Roberts Victor and can be strongly metasomatized (e.g., Greau et al., 2011), while Group II eclogites are generally very fresh, but are much rarer. Kyanite-bearing eclogites, such as the samples in this study, are interlayered with bimineralic Group I eclogites and are thus affiliated with this group, although other classifications distinguish them as a separate group (Huang et al., 2012). Some kyanite-bearing eclogites are grospydites (**gros**sular–**py**roxene–**di**sthene rocks; Sobolev, 1977), distinguished by very Al-rich bulk compositions and garnets with >50 mol% grossular component.

3. MATERIALS AND METHODS

3.1. Samples and petrography

Five kyanite-bearing layered eclogites were chosen from a large suite: three are previously unstudied (RV1570, DEJ1, BD1987) and two have been worked on before (RV124: Jacob and Jagoutz, 1994; BD1168: named 'sample 6913' in Lappin and Dawson, 1975). All samples show modal and compositional layering and either contain a kyanite-bearing part as a layer irregularly sandwiched between bimineralic layers (Fig. 1) or more diffuse layers with kyanites irregularly distributed throughout the rock (DEJ1). The kyanite-bearing areas in each sample except for DEJ1 contain a reaction zone towards the bimineralic sections, in

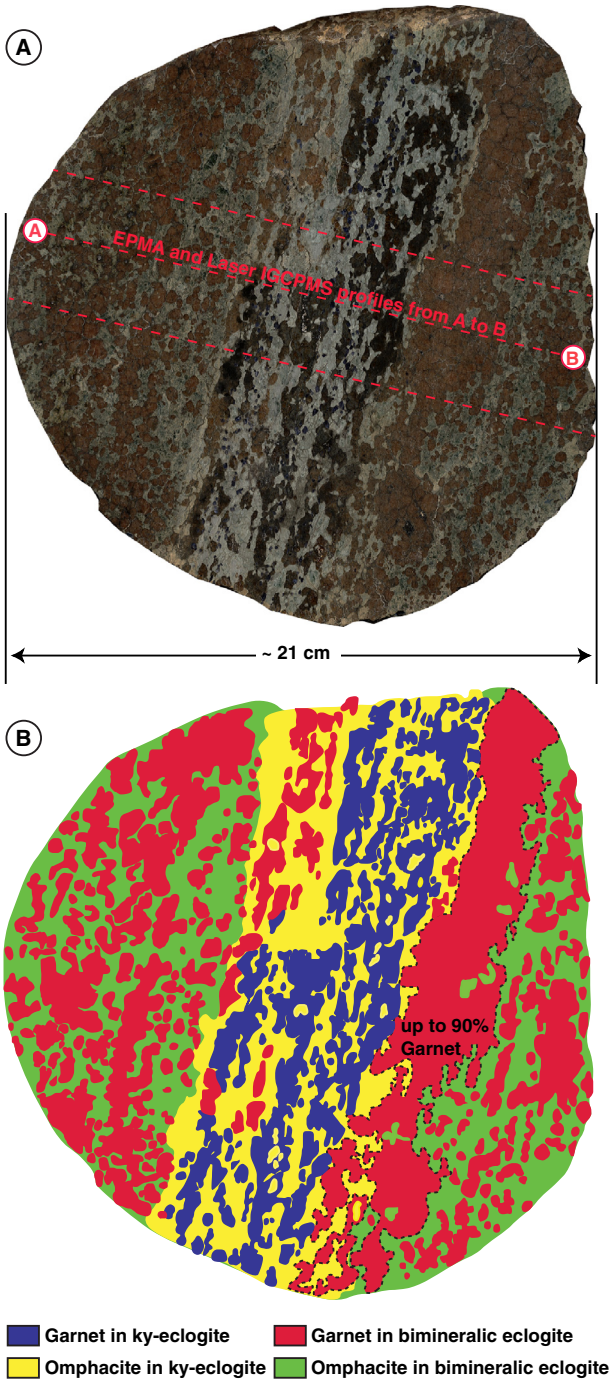

Fig. 1. (A) Inhomogeneous kyanite-bearing eclogite RV1570 from the Roberts Victor Mine, South Africa. Line A to B shows the location of the measured major and trace elements. (B) Sketch map shows the distribution of the two different generations of garnet and omphacite in the sample. Dashed line delineates a garnet rich layer.

which the kyanites are partly resorbed and are overgrown by garnet (Fig. 2). Sample RV124 is a layered diamondiferous eclogite, which contains kyanite only as inclusions in diamond (Jacob and Jagoutz, 1994). Kyanites in sample DEJ1 are unresorbed (Fig. 2d). Sample sizes and modal mineral proportions in different parts of the samples are given in Table 1. Bimineralic eclogites worldwide typically show mineral modes between approximately 40:60 vol% and 60:40 vol % garnet:cpx (Jacob, 2004). However, more accurate mode estimates are often hampered by large grain sizes and small xenoliths. Our suite of large samples shows that the bimineralic parts typically have heterogeneous modes over the scale of centimeters (Fig. 1), including areas of high modal garnet, in some cases up to 90 vol% (Table 1; Jacob and Jagoutz, 1994). Compared to the bimineralic portions, modal clinopyroxene in the kyanite-bearing portions is consistently higher in all studied samples (Table 1).

Garnets are brownish in color, subhedral and between 3 and 6 mm in size. Clinopyroxenes are similar in size and are interstitial, often anhedral. They are dark green in the bimineralic part and pale-green, strongly altered with small clear cores in the kyanite-bearing layer (Fig. 2). Kyanites are lath-shaped, between 1 and 3 mm in size with kink bands and twinning. They are fresh and angular in the central parts of the kyanite-bearing layers, but, many grains show rounded edges and embayments and most are overgrown by garnet to variable extents in the reaction zone close to the bimineralic parts (Fig. 2). In all samples except DEJ1 the kyanite layer shows a foliation defined by the kyanite laths. Kyanite in BD1168 contains rutile needles, which are deformed across the kink bands. DEJ1 is less altered and shows generally slightly smaller grain sizes than the other samples.

From the rocks in this suite, RV1570 is the largest sample (Fig. 1) and displays the largest mineral chemical compositional range. This sample was chosen for detailed microanalytical work across the complete section shown in Fig. 1 and serves as the best example of a layered kyanite-bearing eclogite in the context of other similar samples for which such detailed analytical work was not possible due to alteration or sample size.

3.2. Methods

All samples except DEJ1 were cut orthogonal to the layering into three (BD1168, RV124, BD1987) or five (RV1570) sections (Table 1). Major and trace element measurements by electron microprobe (EPMA) and Laser Ablation-Inductively Coupled Plasma Mass Spectrometry (LA-ICPMS) were performed on polished thick sections prepared from these rock sections. Oxygen isotopes were determined either from handpicked (by Laser Fluorination) or mounted (by Secondary Ion Mass Sepctrometry, SIMS) grains from the rock sections as well as *in situ* by SIMS on a thin section of DEJ1. Infrared Sepctroscopy (FTIR) of the kyanites in RV1570 was performed on a doubly polished section following the methods described in Bell et al. (2004).

A JEOL JXA 8900 RL microprobe at the Johannes Gutenberg University, Mainz (Germany) was used to determine the major element compositions of all phases using wavelength dispersive analysis and a range of natural and synthetic standards. The data were corrected using the CIT-ZAF procedure (Armstrong, 1995). Detection limits were generally between 0.01 and 0.07 wt.% (15 kV, 12 nA, 2 μm beam size).

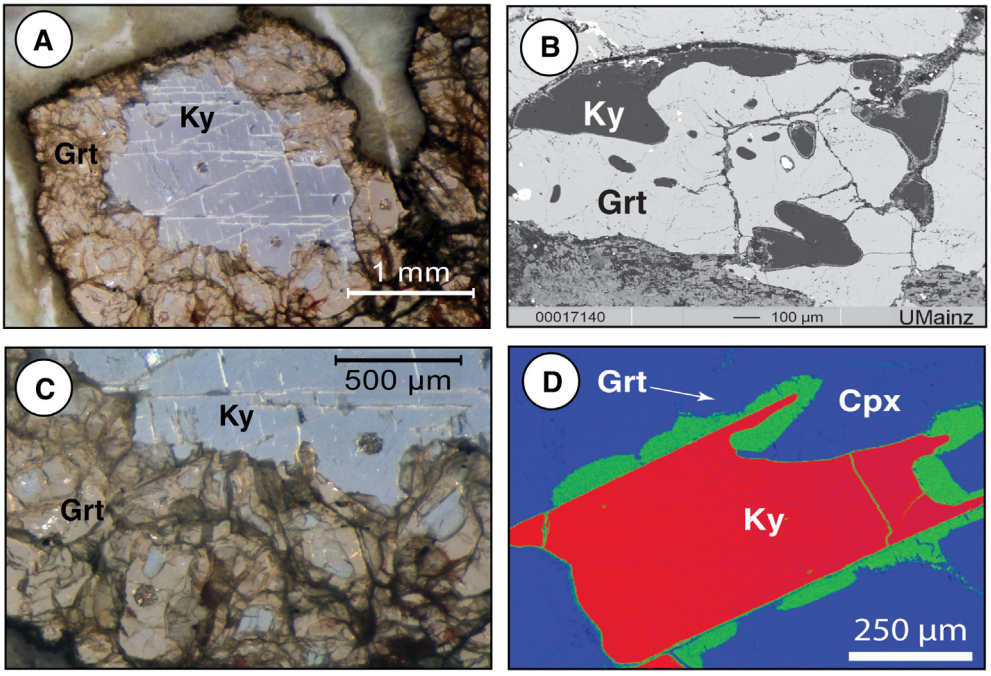

Fig. 2. Replacement textures in kyanite-bearing eclogites. (a) kyanite resorbed and overgrown by garnet; (b) backscattered secondary electron image of kyanite grains (dark gray) in RV 1570 resorbed by garnet (light gray) adjacent to altered cpx (bottom of image); (c) close-up of the lower edge of the kyanite in (a) showing small resorbed remnants of the large kyanite grain embedded in newly-formed fine-grained garnet (sample BD1168); (d) EPMA aluminum distribution map showing an embayed kyanite grain (red) in sample DEJ1 set in a matrix of cpx (blue) with garnet (green) replacing cpx along the kyanite grain boundaries. (For interpretation of the references to colour in this figure legend, the reader is referred to the web version of this article.)

Table 1
Summary of sample sizes, petrography and modal proportions.

	RV1570		BD1168			RV124			DEJ1	BD 1987	
Length (cm)	21 cm		11 cm			35 cm			14 cm	18 cm	
Sections	Bimin-layer	Ky-layer	1	2	3	A1	A3	A6		A	B
Petrography	Gt + cpx	Gt + cpx + ky	Gt + cpx	Gt + cpx + ky	Gt + cpx	Gt + cpx	Gt + cpx	Gt + cpx	Gt + cpx + ky	Gt + cpx	Gt + cpx + ky
Mode (vol%)	34:66	48:50:2	55:45	45:45:10	55:45	45:55	60:40	90:10	32:56:12	50:50	40:40:20
Others			Rutile	Rutile			Graph	Dia		Rutile	Rutile

Trace elements were analyzed by Laser Ablation ICP-MS using a Agilent 7500ce quadrupole ICP-MS coupled with an esi/NWR193 nm wavelength excimer laser following methods described in Jacob (2006). Ablation was carried out at 6.4 J/cm^2 and 10 Hz, using He as the carrier gas. All measurements were performed on polished thick sections using spot size diameters of 100 µm or 60 µm. GLITTER 4.0 software (Griffin et al., 2008) was used for data reduction with NIST SRM 612 (Jochum and Nehring, 2006) as the external standard and ^{43}Ca as the internal standard using values for CaO from the electron microprobe analyses. USGS glass BCR2-G was measured as an unknown in every session as quality control and always yielded values within 10% of the published values (Table A1). Care was taken to analyze only unaltered and crack-free parts of grains. To ensure this, the target area was checked in reflected and in transmitted light prior to each spot analysis. The time-resolved signals for each individual analysis were screened for inclusions or cracks (identified by spikes in the time-resolved signal) and affected parts or complete analyses were discarded accordingly.

Sample preparation and secondary ion mass spectrometry (SIMS) were carried out at the Canadian Centre for Isotopic Microanalysis (CCIM), University of Alberta. Garnet mineral separates from samples BD1168 (CCIM #S3026), RV124 (S3029), and RV1570 (S3032) and CCIM garnet reference materials (RMs) S0068 (Gore Mountain Ca-Mg-Fe garnet) and S0088B (grossularite) were mounted and mid-sections exposed in a 25 mm diameter epoxy assembly (M1284) using diamond grits. A second 25 mm mount (M1313) was prepared comprising small pieces of thin section from DEJ1 (S3174), the garnet RMs mentioned

previously, and kyanite RM SRV1 (S0346, Smyth and Hatton, 1977). The mounts were cleaned with a lab soap solution, and de-ionized H_2O. Prior to scanning electron microscopy (SEM), the mounts were coated with 7 nm of high-purity Au. SEM characterization was carried out with a Zeiss EVO MA15 instrument using beam conditions of 20 kV and 3–4 nA. A further 25 nm of Au was subsequently deposited on the mounts prior to SIMS analysis.

Oxygen isotopes (^{18}O, ^{16}O) in garnet and kyanite were analyzed using a Cameca IMS 1280 multicollector ion microprobe. Garnet analytical methods and RMs are detailed by Ickert and Stern (2013), and are briefly summarized here. A $^{133}Cs^+$ primary beam was operated with impact energy of 20 keV and beam current of ~2.5 nA. The ~12 μm diameter probe was rastered (20 × 20 μm) for 30 s prior to acquisition, and then 5 × 5 μm during acquisition, forming rectangular analyzed areas ~15 × 18 μm across and ~2 μm deep. The normal incidence electron gun was utilized for charge compensation. Negative secondary ions were extracted through 10 kV into the secondary (Transfer) column. Transfer conditions included a 122 μm entrance slit, a 5 × 5 mm pre-ESA (field) aperture, and 100× sample magnification at the field aperture, transmitting all regions of the sputtered area. No energy filtering was employed. The mass/charge separated oxygen ions were detected simultaneously in Faraday cups L'2 ($^{16}O^-$) and H'2 ($^{18}O^-$) at mass resolutions (m/Δm at 10%) of 1900 and 2275, respectively. Secondary ion count rates for $^{16}O^-$ and $^{18}O^-$ were 2.5–3.5 × 10^9 and 5–7 × 10^6 counts/s utilizing 10^{10} Ω and 10^{11} Ω amplifier circuits, respectively. Faraday cup baselines were measured at the start of the analytical session. A single analysis took 4 min, including pre-analysis primary beam implantation, automated secondary ion tuning, and 75–90 s of continuous peak counting.

For garnet analysis, instrumental mass fractionation (IMF) was monitored by repeated analysis of S0068 (UAG) and S0088B with $\delta^{18}O_{VSMOW} = +5.72$ and +4.13, respectively. One analysis of S0068 and S0088B were taken after every 4 and 8 unknowns, respectively. The data set of $^{18}O^-/^{16}O^-$ for S0068 garnet was processed collectively for each of three analytical sessions (IP14051, IP15011, IP15011B), yielding standard deviations of 0.07–0.08‰ after correction for systematic within-session drift (<0.3‰). Overall IMF was +3‰ to +5.5‰. Data for S0088B and unknowns were first IMF corrected to S0068 garnet, and then further corrected according to their measured Ca numbers (Ca/[Ca + Mg + Fe]) using the methods outlined by Ickert and Stern (2013). For session IP14051, the quadratic matrix calibration curve parameters reported in Ickert and Stern (2013) were utilized *a priori*, as the results from S0088B were highly accurate without modification ($\delta^{18}O_{VSMOW} = +4.15 \pm 0.06$, MSWD = 0.56, N = 19). For session IP15011, the calibration parameters were scaled to fit S0088B to its reference value. The 95% confidence uncertainty estimates for $\delta^{18}O_{VSMOW}$ for garnet averaged ±0.28‰, and include errors relating to within-spot counting statistics, between-spot (geometric) effects, correction for instrumental mass fractionation, and matrix effects relating to Ca-numbers determined by electron microprobe on spots adjacent to the SIMS pits.

IMF for kyanite was determined and corrected as for garnet by repeated analysis of SRV-1 kyanite with $\delta^{18}O_{VSMOW} = +7.98$ (Sharp et al., 1992). Average per spot analytical uncertainty is ±0.20‰. Major- and trace-element compositions of garnets were determined at the Unversity of Alberta using a JEOL-8900 SuperProbe. Electron beam conditions included an accelerating voltage of 20 kV, a 20 nA beam current and 1 μm beam diameter. Raw X-ray counts were converted to elemental concentrations using natural garnet standards. Detection limits include 250 ppm for P_2O_5, 200 ppm for Na_2O and <100 ppm for all other oxides. Methods employed for Laser Fluorination analysis can be found in Mattey and MacPherson (1993).

3.3. Mass balance approach

To quantify the kyanite-out reaction observed in these samples a mass balance was carried out for sample RV1570 based on its modal mineralogy determined on the polished face of the sample (Fig. 1) with the free software ImageJ (Rusband, 2009, Table A2). Major element compositions of cpx and garnet (Tables 2 and A2) were selected for mineral pairs in the kyanite-bearing part that gave highest *P* and *T* estimates (800 °C, 5.5 GPa using Perple_X, see below) and for mineral pairs giving peak metamorphic conditions in the bimineralic part of the sample. These analyses were then divided by the molar wt% of each oxide and recalculated to 1 Si formula unit (Table A2a). The molar proportions of each mineral were calculated relative to the molar weight of Si, the volume proportions, and the mass and density of each mineral (Table A2b). Starting conditions for balancing the kyanite-out reaction were chosen as 1 (i.e. the entire rock volume homogeneously contained kyanite), while the end conditions were set to 0.7 reflecting the remaining volume of kyanite in RV1570.

The mass balance approach for the formation of garnet in the bimineralic eclogite (Table A2c) is based on the following two mineral endmember scenarios: Case (I) all garnet in the bimineralic part was formed by transformation of Na-rich clinopyroxene in the kyanite bearing eclogite and case (II) all garnet in the bimineralic part originates from Grs-rich garnet in the kyanite-bearing part. A separate mass balance approach for omphacite in the bimineralic eclogite (Table A2d) follows an analogous scenario: Case (I) all omphacite in the bimineralic eclogite was formed from Na-rich cpx in the kyanite-bearing part and, case (II) all omphacite in the bimineralic eclogite was formed from Grs-rich garnet in the kyanite-bearing eclogite.

4. RESULTS

4.1. Major elements

Garnet (grt) and clinopyroxene (cpx) compositions in the kyanite-bearing and bimineralic eclogites span a large range (Figs. 3A and A1). Primary garnets associated with lath-shaped, unresorbed kyanites, are high in CaO and

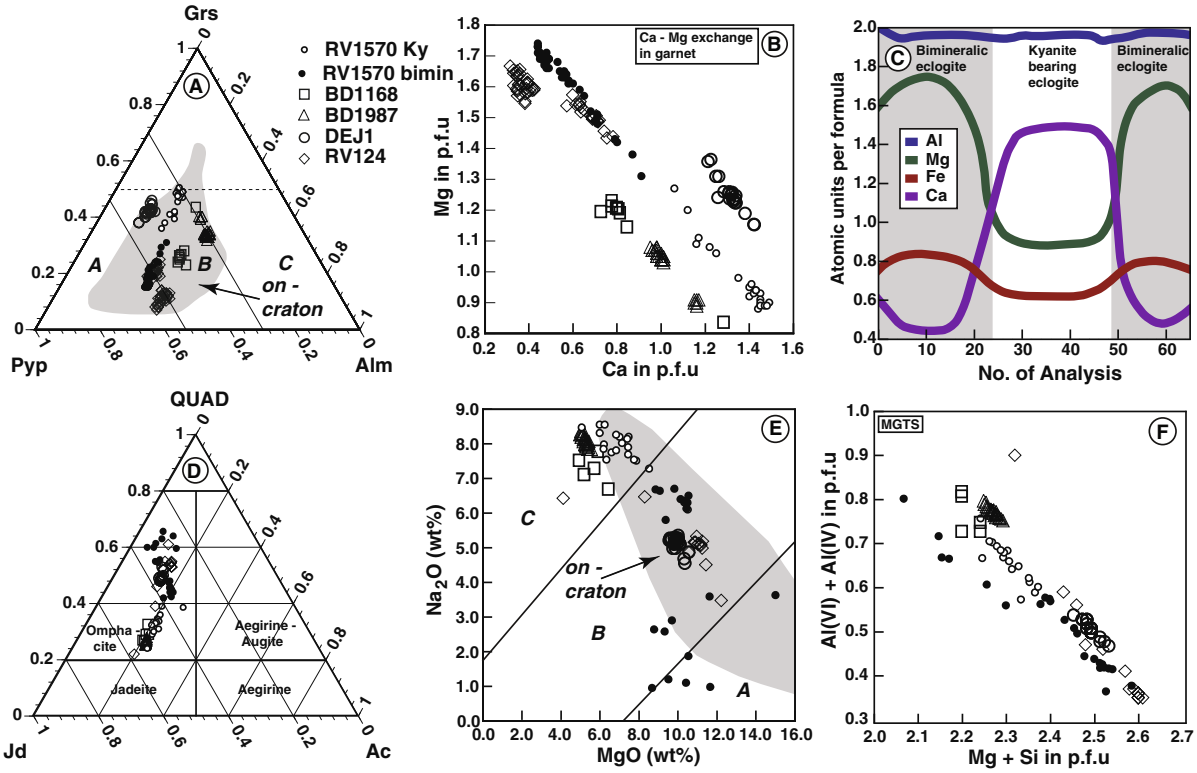

Fig. 3. (A) Trilateral garnet composition diagram after Taylor and Neal (1989). (B) Ca-Mg exchange vector in garnet. (C) Garnet microprobe line scan across sample RV1570 showing the distribution of the main elements Al, Mg, Fe and Ca in garnets from the ky bearing- and the bimineralic eclogite. (D) Pyroxene classification triangle after Morimoto et al. (1988), showing the composition of omphacite in kyanite-bearing and bimineralic eclogites. (E) Cpx composition diagram after Taylor and Neal (1989). (F) Mg Tschermak exchange in cpx.

low in MgO compared to overgrowths on garnets and those from bimineralic areas. Clinopyroxenes are jadeite-rich omphacites in the kyanite-bearing parts and QUAD-rich omphacites in the bimineralic areas. In contrast to the grain-to-grain inhomogeneity, within grain zonation was not observed in any of the samples, not even in the small garnet grains overgrowing and rimming the kyanite (Fig. 2).

4.1.1. Garnets

All garnets overlap with literature data for Roberts Victor eclogites (Fig. 3A; gray field). Garnets in RV 1570 show the largest compositional variation within the sample set (Fig. 3A–C), namely from $X_{Grs} = \sim 0.15$, $X_{Pyp} = \sim 0.48$, $X_{Alm} = \sim 0.24$ in the bimineralic part to $X_{Grs} = \sim 0.50$, $X_{Pyp} = \sim 0.30$, $X_{Alm} = \sim 0.13$ in the kyanite-bearing part (Table 2a and A3). The main exchange vector in garnets from all samples is controlled by the Mg–Ca exchange (Fig. 3B), while X_{Alm} is rather constant (in RV1570 $X_{Alm} = \sim 0.13$ to ~ 0.22). Only the grossular-poor garnets in the bimineralic part of sample RV124 show slightly higher almandine contents (Fig. 3A). Some garnets in the kyanite-bearing part of sample RV1570 are grospyditic with grossular >50% (Fig. 3A; Sobolev, 1977). Concentrations of TiO_2 and Cr_2O_3 are low and range between 0.1 and 0.4 wt% for TiO_2 and are around 0.1 wt% for Cr_2O_3.

Using the classification of Taylor and Neal (1989), garnets in RV1570 straddle all three groups with garnets in the kyanite-bearing part falling in Group C, those from the reaction zone between kyanite-bearing and bimineralic layers in Group B, and those from the bimineralic area in Group A (Fig. 3A). Most garnets from sample BD1168 fall in Group B, except for one that classifies as Group C. All garnets in sample BD1987 plot on the boundary between Group B and C. Garnets in sample DEJ1 all fall in Group B, and garnets in sample RV124 are Group A and B.

4.1.2. Clinopyroxenes

All clinopyroxenes in the samples are omphacites (Morimoto et al.,1988), but some have fassaitic compositions. Fassaites are high CaO, Al_2O_3 clinoproxenes, originally discovered in meteorites but also described from peraluminous eclogites (Bloxam and Allen, 1960), including BD1168 (Lappin and Dawson, 1975). Omphacites in the kyanite portion of RV1570 show the highest jadeite component ($X_{Jd} = \sim 0.41$ to ~ 0.53) and consequently lower ratios of X_{QUAD} between ~ 0.24 and ~ 0.39 (Fig. 3D). In the reaction zone between the kyanite-bearing and bimineralic portions (Fig. 3F), X_{Jd} is between ~ 0.34 and ~ 0.39 and X_{QUAD} between ~ 0.42 and ~ 0.48 (Fig. 3D; Tables 2b and A3). Two types of omphacites were observed in the bimineralic zone, namely diopside-rich ones and fassaites included as small relics in them (Tables 2c and A3). Both types show elevated QUAD components, ranging between ~ 0.54 and ~ 0.65 (Fig. 3D) and consequently the lowest X_{Jd} between ~ 0.25 and ~ 0.35, but the fassaitic clinopyroxenes have

Table 2a
Representative average major element compositions of garnets.

	RV1570	RV1570	RV1570	RV1570	RV1570	RV1570	BD1168	BD1168[b]	RV124A1	RV124A6	DEJ1	DEJ1	BD1987	BD1987
Paragenesis	Ky	Bi	Tr	Tr	Tr	Tr	Ky	Bi	Bi	Ky[a]	Ky	Tr	Bi	Ky
n	5	5	1	1	1	1	5	5	5	5	5	1	5	5
SiO_2	40.64	41.54	41.36	40.98	40.44	41.51	40.08	39.68	40.92	40.68	41.54	40.51	40.31	39.96
TiO_2	0.36	0.27	0.33	0.33	0.36	0.28	0.18	0.29	0.27	0.28	b.d.l.	b.d.l.	0.41	0.41
Al_2O_3	22.55	22.70	22.59	22.56	22.32	22.99	21.98	23.33	22.31	22.54	24.23	22.88	23.52	23.49
Cr_2O_3	b.d.l.	b.d.l.	b.d.l.	b.d.l.	0.14	b.d.l.	b.d.l.	b.d.l.	b.d.l.	b.d.l.	b.d.l.	b.d.l.	0.21	b.d.l.
FeO	10.40	13.67	12.64	11.65	11.54	12.85	14.10	15.25	16.82	13.06	7.71	7.60	14.80	14.23
MnO	0.20	0.34	0.24	0.22	0.18	0.24	0.24	0.42	0.47	0.24	0.19	0.18	0.15	0.35
MgO	8.10	15.85	12.11	10.10	9.78	13.28	7.94	10.80	15.08	13.35	11.61	10.56	9.76	8.20
CaO	18.40	5.84	11.68	14.86	15.45	10.27	16.78	10.06	4.43	9.39	16.37	18.13	12.32	14.63
Na_2O	0.13	0.12	0.15	0.14	0.14	0.16	0.14	0.13	0.12	0.12	b.d.l.	b.d.l.	0.15	0.15
K_2O	b.d.l.	b.d.l.	b.d.l.	b.d.l.	b.d.l.	b.d.l.	b.d.l.	b.d.l.	b.d.l.	b.d.l.	b.d.l.	b.d.l.	b.d.l.	b.d.l.
Total	100.78	100.34	101.19	100.86	100.25	101.67	101.43	100.01	100.55	99.67	101.72	100.02	101.63	101.44

[a] Kyanite present as inclusions in diamond only,
[b] Data from Lappin and Dawson (1975).

Table 2b
Representative average major element compositions of clinopyroxenes.

	RV1570	RV1570	RV1570	RV1570	RV1570	RV1570	BD1168	BD1168[b]	RV124A1	RV124A6	DEJ1	BD1987	BD1987
Paragenesis	Ky	Bi	Tr	Tr	Tr	Tr	Ky	Bi	Bi	Ky[a]	Ky	Bi	Ky
n	5	5	1	1	1	1	5	5	5	1	26	10	17
SiO_2	56.45	55.33	56.14	55.64	55.30	55.63	56.43	56.8	56.62	56.19	54.97	56.16	56.22
TiO_2	0.33	0.37	0.33	0.31	0.30	0.28	0.32	0.17	0.38	0.30	b.d.l.	0.32	0.32
Al_2O_3	15.55	10.52	11.35	16.64	17.14	16.89	18.34	17.14	8.38	14.15	12.13	18.27	18.70
Cr_2O_3	0.11	b.d.l.	0.13	b.d.l.	b.d.l.	b.d.l.	b.d.l.	b.d.l.	b.d.l.	b.d.l.	b.d.l.	b.d.l.	b.d.l.
FeO	2.08	3.51	3.11	1.74	1.55	1.62	2.38	2.24	5.12	2.21	1.15	2.24	2.19
MnO	b.d.l.	b.d.l.	b.d.l.	b.d.l.	b.d.l.	b.d.l.	b.d.l.	b.d.l.	0.10	b.d.l.	b.d.l.	b.d.l.	b.d.l.
MgO	6.84	10.32	9.53	6.47	6.35	6.38	5.62	6.19	11.10	8.28	9.91	5.37	5.15
CaO	10.64	13.36	12.57	11.82	11.42	11.08	9.30	10.12	13.19	11.78	15.99	8.85	8.60
Na_2O	8.29	6.29	6.67	7.16	7.77	7.88	7.29	7.25	5.12	6.47	5.10	7.97	8.18
K_2O	b.d.l.	b.d.l.	b.d.l.	b.d.l.	b.d.l.	b.d.l.	b.d.l.	b.d.l.	b.d.l.	b.d.l.	b.d.l.	b.d.l.	b.d.l.
Total	100.40	99.97	99.99	99.96	100.00	99.99	99.83	99.88	99.25	99.60	99.40	99.23	99.43

[a] kyanite present as inclusions in diamond only,
[b] data from Lappin and Dawson (1975).

Table 2c
Representative average major element compositions of fassaitic clinopyroxenes and diopside hosts.

	RV1570	RV1570	RV1570	RV1570	RV1570	RV1570	RV1570	RV1570
Paragenesis	Bi	Bi	Bi	Bi	Bi	Bi	Bi	Bi
n	1	1	1	1	1	1	5	5
SiO_2	48.24	43.14	45.99	44.89	44.45	46.11	47.50	52.28
TiO_2	0.75	0.57	2.00	0.50	0.62	1.43	1.05	0.34
Al_2O_3	14.32	18.46	15.56	15.23	16.62	15.62	13.07	8.53
Cr_2O_3	b.d.l.	b.d.l.	b.d.l.	b.d.l.	b.d.l.	b.d.l.	b.d.l.	b.d.l.
FeO	5.07	7.33	5.23	8.58	7.26	5.29	5.66	5.51
MnO	b.d.l.	b.d.l.	b.d.l.	b.d.l.	b.d.l.	b.d.l.	b.d.l.	b.d.l.
MgO	9.69	8.67	8.77	10.41	9.51	9.32	10.53	11.62
CaO	19.44	20.60	19.74	17.22	20.45	20.04	20.60	17.15
Na_2O	2.90	0.95	2.64	1.10	1.20	2.58	1.87	3.59
K_2O	b.d.l.	b.d.l.	b.d.l.	b.d.l.	b.d.l.	b.d.l.	b.d.l.	b.d.l.
Total	100.86	99.96	100.15	98.92	100.44	100.67	100.47	99.42

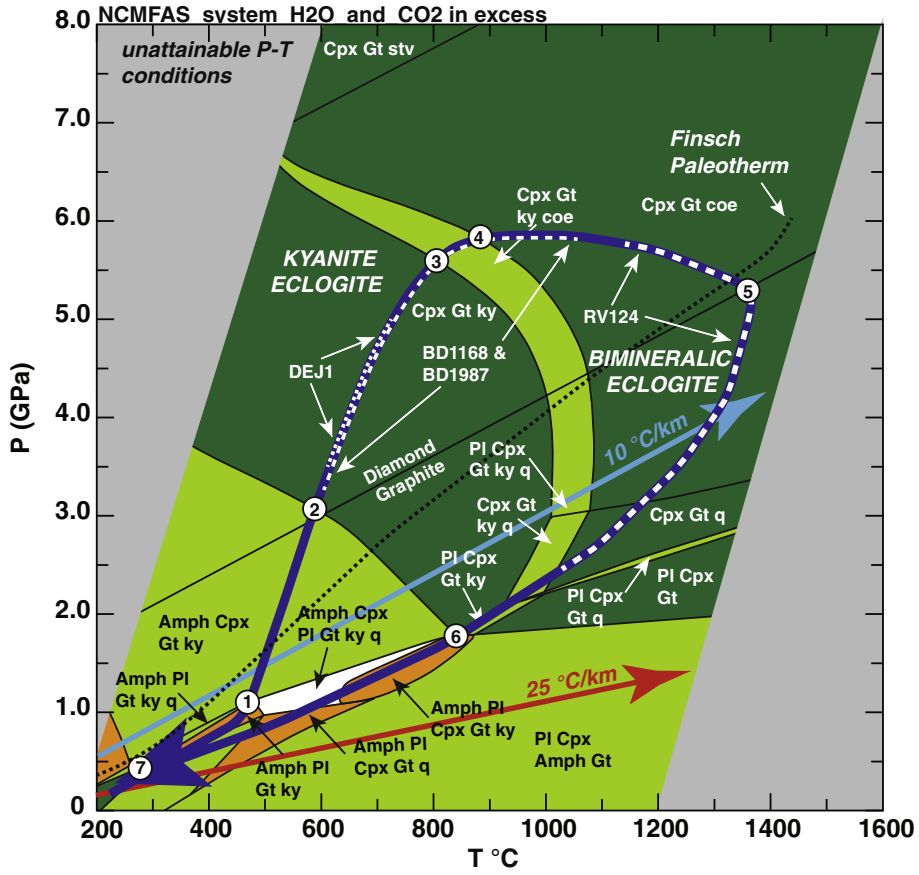

Fig. 4. *P-T* pseudosection with a seven stage *P-T* path for sample RV1570 (stages indicated by circled numbers from 1 to 7) in the NCMFAS system with H_2O and CO_2 in excess. Peak metamorphic mineral assemblage is gt, cpx and coe. Dashed white lines with sample names indicate *P-T* conditions corresponding to other samples in this study projected on the *P-T* path for RV 1570. *P-T* conditions for sample BD1168 were calculated including data in Lappin and Dawson (1975). Light blue arrow represents a typical subduction gradient with 10 °C/km, red arrow is a typical collision geotherm with 25 °C/km. Also plotted are the local paleogeotherm for the Finsch peridotite xenoliths (black dotted line; Mather et al., 2011) and the diamond-graphite boundary (Day, 2012). See text for discussion of the numbered PT points.

higher Al_2O_3, CaO and lower SiO_2 concentrations compared to their diopsidic host.

All clinopyroxenes display a coupled substitution between the Ca-Tschermak ($Ca + Si \leftrightarrow 2Al$) and Mg-Tschermak ($Mg + Si \leftrightarrow 2Al$, (Figs. 3F and A1)) exchanges, as well as coupled substitution of $Ca + Si \leftrightarrow Na + Mg + Al$ exchange. In RV1570, omphacite associated with kyanite shows lower $(Ca + Si)/2Al$ (Fig. A1) and higher $(Mg + Si)/2Al$ (Fig. 3F) ratios than that in the bimineralic zone due to higher jadeite contents in the kyanite-bearing part. RV124 has a similar compositional range with the same exchange vectors as sample RV1570, while cpx in DEJ1 is

compositionally homogenous and similar to omphacites of the transitional zone between kyanite-bearing and kyanite-free parts in RV1570. Omphacites in BD1168 and BD1987 are most similar to those from the kyanite-bearing part in RV1570. Classification of the clinopyroxenes using the scheme of Taylor and Neal (1989) results in a spread across the three groups similar to that for the co-existing garnets (Fig. 3E).

4.1.3. Geothermobarometry

Prograde, peak and retrograde metamorphic pressure and temperature conditions were calculated with a *P-T* pseudosection based on the bulk rock composition of sample RV1570. Sample RV1570 was used because it shows the largest variation in mineral chemical endmembers of grt and cpx and therefore allows the construction of a complete *P-T* loop. All other samples, while sharing the same *P-T* history, are representative only for restricted parts of the *P-T* loop and their calculated *P-T* conditions are plotted on the *P-T* path for RV1570 in Fig. 4.

We used the following approach for calculating the *P-T* conditions: Measured major element compositions were used to roughly screen and identify the different *P-T* stages preserved in RV1570 using the geothermobarometer of Simakov (2008) and additionally the geothermometer of Ellis and Green (1979) as well as by projecting the temperatures derived from Ellis and Green (1979) and Simakov (2008) on the local paleogeotherm (Bell et al., 2003; Mather et al., 2011). Compared to grts in mantle eclogites, and in kyanite-bearing samples in particular, cpx in these rocks is often affected by multistage metasomatism and alteration. As in peridotite xenoliths, these secondary changes to mineral compositions result in disequilibrium assemblages and increase uncertainties in geobarometry (Mather et al., 2011). For the best circumvention of this issue, we used measured major element garnet compositions screened to represent different *P-T* stages to calculate model equilibrium cpx compositions using Simakov (2008). PT conditions with resulting uncertainties are given in Table S3.

These cpx compositions were checked against the dataset of measured major elements for RV1570, and grains with major element compositions as close as possible to the model equilibrium compositions were identified and paired with garnets as inputs for the Perple_X model. Some cpx analyses had to be slightly adjusted, namely by changing X_{Mg} by 1–3 wt% to reconcile them with the model equilibrium cpx compositions. Results of this modeling step were cross-checked with the geobarometer of Beyer et al. (2015) to ensure they fall in the correct *P-T* realm as in the screening step at the start. Finally, the predicted modal abundances of the garnets and clinopyroxenes in the kyanite bearing eclogite as well as in the bimineralic eclogite calculated with Perple_X were crosschecked with the measured modal abundance (planimetry) from sample RV1570 (Figs. 5 and A2a and b).

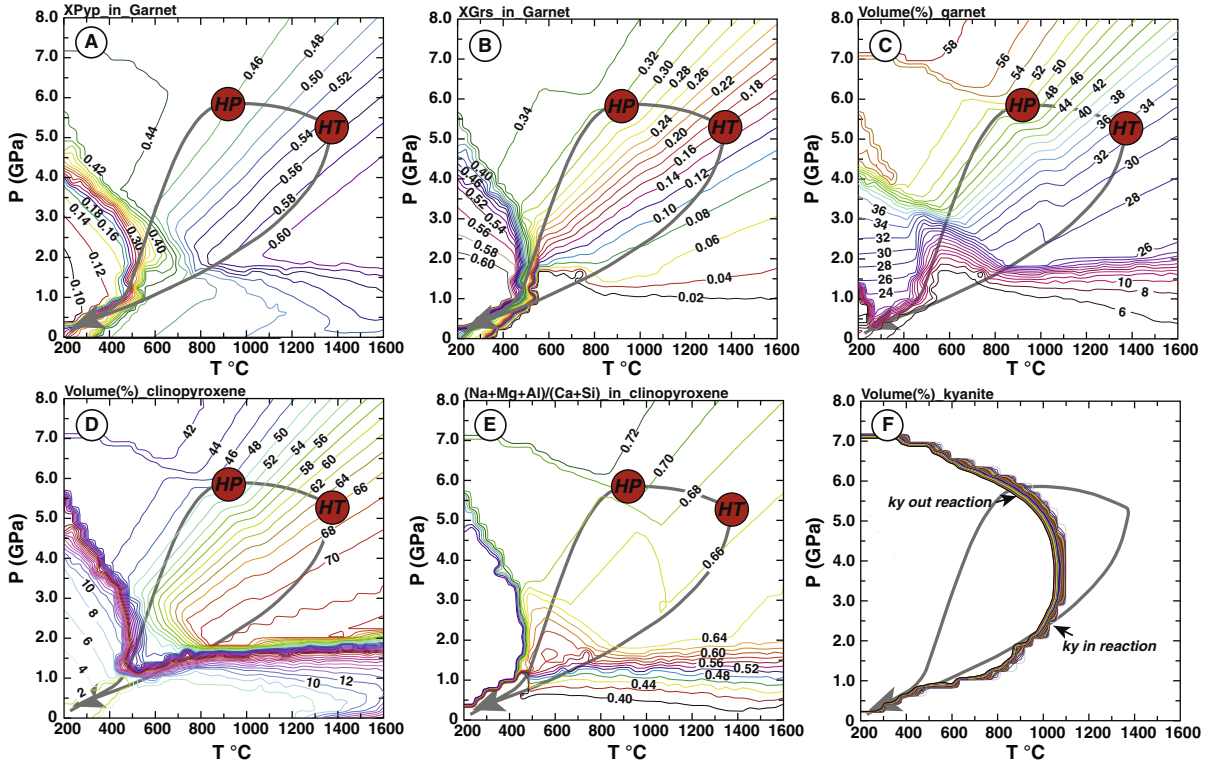

Fig. 5. (a and b) Variations in X_{Prp} and X_{Grs} during prograde, peak and retrograde metamorphism. (c) Volumetric calculations of garnet indicate that garnet forms continuously as pressure increases and is consumed afterwards. (d) Volumetric calculations of cpx show that cpx is formed along the computed *P-T* loop; (e) Na + Al + Mg ↔ Ca + Si exchange in cpx; (f) Volumetric calculation of kyanite shows that kyanite is consumed during prograde metamorphism close to the pressure maximum, and will be re-stabilized during retrograde metamorphism.

Table 3
Representative average trace element analyses in ppm of typical garnet and clinopyroxene compositions from petrographically different sections in each sample.

	RV1570 gt	RV1570 cpx	RV1570 gt	RV15701 cpx	BD1168 grt	BD1168 cpx	BD1168 grt	BD1168 cpx
Paragenesis	ky	ky	bi	bi	ky	ky	bi	bi
n	22	6	17	8	1	1	1	6
Li	2.30	26.4	1.43	11.0	n.m.	n.m.	n.m.	n.m.
Th	0.012	<0.02	0.016	0.009	0.015	<0.001	<0.001	<0.001
U	0.010	<0.01	<0.03	0.009	0.004	0.002	0.0026	<0.001
Nb	0.023	0.023	0.038	0.044	0.009	0.004	0.025	0.020
Ta	0.010	0.013	0.009	<0.02	<0.001	0.004	0.001	0.003
La	0.054	0.163	0.055	0.730	0.042	0.108	0.038	0.186
Ce	0.567	0.762	0.210	3.25	0.463	0.625	0.404	0.955
Pr	0.222	0.143	0.077	0.626	0.274	0.151	0.160	0.188
Sr	7.64	128	1.04	199	4.79	46.6	1.57	65.4
Nd	2.23	0.748	0.871	3.38	3.80	0.654	1.80	1.071
Sm	0.979	0.152	0.720	0.627	2.90	0.200	1.33	0.263
Zr	13.98	3.23	23.6	18.2	52.9	8.01	28.4	7.559
Hf	0.270	0.171	0.491	1.12	0.927	0.443	0.576	0.48
Eu	0.755	0.054	0.39	0.219	1.34	0.066	0.788	0.088
Ti	22,220	1586	1520	2240	1799	1918	1799	1918
Gd	1.04	0.067	1.44	0.511	3.95	0.095	2.85	0.234
Tb	0.184	0.011	0.318	0.061	0.616	0.018	0.758	0.027
Dy	1.24	0.097	2.34	0.294	3.34	0.103	5.73	0.106
Y	6.810	0.081	13.6	0.965	17.0	0.251	34.1	0.433
Ho	0.274	0.009	0.540	0.044	0.626	0.009	1.33	0.013
Er	0.758	<0.05	1.52	0.091	1.74	0.027	3.78	0.038
Tm	0.114	0.008	0.219	0.019	0.251	0.003	0.533	0.004
Yb	0.795	<0.1	1.55	0.087	1.20	0.004	3.41	0.024
Lu	0.123	0.010	0.223	0.011	0.194	0.001	0.510	0.002
Cr	609	474	384	572	n.m.	n.m.	n.m.	n.m.
Mn	1590	130	2820	422	n.m.	n.m.	n.m.	n.m.
Co	55.2	20.8	65.4	25.2	n.m.	n.m.	n.m.	n.m.
Ni	63.0	326	55.6	324	n.m.	n.m.	n.m.	n.m.
Zn	74.0	38.7	70.5	47.5	n.m.	n.m.	n.m.	n.m.
V	74.9	135	80.5	290	60.8	124	94.6	237
Sc	34.4	10.1	40.1	12.3	35.9	4.45	48.8	6.01
P	100	23.8	173	56.6	n.m.	n.m.	n.m.	n.m.
	RV124 grt	RV124 grt	RV124 cpx	DEJ1 grt	DEJ1 cpx	BD1987 grt	BD1987 gt	BD1987 cpx
Paragenesis	(ky)	bi	bi	ky	ky	ky	bi	bi
n	1	1	1	6	7	1	1	1
Li	n.m.	n.m.	n.m.	n.m.	n.m.	n.m.	n.m.	n.m.
Th	<0.01	<0.001	<0.001	0.011	0.022	<0.01	0.006	<0.02
U	0.011	0.003	<0.01	0.013	<0.02	0.009	0.009	<0.02
Nb	<0.03	0.036	0.026	0.022	0.046	0.045	0.068	0.014
Ta	<0.02	<0.01	<0.02	0.002	<0.02	<0.02	0.009	0.012
La	<0.02	0.022	0.465	0.322	2.41	0.094	0.209	0.191
Ce	0.625	0.235	2.16	2.42	5.60	1.12	1.04	1.18
Pr	0.298	0.085	0.441	0.401	0.395	0.454	0.320	0.205
Sr	2.24	1.12	182	5.56	5.60	3.48	3.38	76.5
Nd	2.76	0.857	2.70	1.66	0.841	4.90	3.40	1.02
Sm	1.60	0.692	0.579	0.245	0.067	3.32	2.37	0.210
Zr	12.9	22.5	12.4	2.02	0.841	63.8	47.6	6.26
Hf	0.238	0.569	0.782	0.051	0.067	1.33	0.889	0.456
Eu	0.861	0.441	0.175	0.319	0.020	1.66	1.05	0.067
Ti	1619	0.162	0.222	300	240	0.276	0.277	0.198
Gd	1.71	2.01	0.450	0.185	<0.01	5.09	4.07	0.142
Tb	0.263	0.377	0.044	0.033	0.009	1.01	0.899	0.015
Dy	1.48	2.76	0.199	0.215	<0.01	5.70	5.91	0.089
Y	6.82	13.0	0.643	1.35	0.029	23.5	33.5	0.312
Ho	0.273	0.487	0.035	0.045	0.012	0.964	1.17	0.010
Er	0.722	1.37	0.059	0.183	<0.01	1.92	2.77	0.022
Tm	0.079	0.174	<0.01	0.025	<0.02	0.186	0.335	<0.01
Yb	0.708	1.13	0.021	0.215	<0.01	1.04	1.86	<0.01

(*continued on next page*)

Table 3 (*continued*)

	RV124 grt	RV124 grt	RV124 cpx	DEJ1 grt	DEJ1 cpx	BD1987 grt	BD1987 gt	BD1987 cpx
Lu	0.084	0.175	<0.01	0.038	<0.01	0.114	0.238	<0.01
Cr	n.m.	n.m.	n.m.	n.m.	n.m.	n.m.	n.m.	n.m.
Mn	n.m.	n.m.	n.m.	n.m.	n.m.	n.m.	n.m.	n.m.
Co	n.m.	n.m.	n.m.	n.m.	n.m.	n.m.	n.m.	n.m.
Ni	n.m.	n.m.	n.m.	n.m.	n.m.	n.m.	n.m.	n.m.
Zn	n.m.	n.m.	n.m.	n.m.	n.m.	n.m.	n.m.	n.m.
V	68.7	62.4	197	21.9	43.72	52.4	77.3	236
Sc	30.6	34.1	8.00	27.1	<10	23.8	32.1	4.83
P	n.m.	n.m.	n.m.	n.m.	n.m.	n.m.	n.m.	n.m.

These *P-T* values and modal abundances were used to inform the Perple_X modeling on the upper and lower *P-T* conditions to calibrate the volatile-bearing phase fields of the pseudosection. A value of 0.9 for a starting X_{H2O} value was used, constrained by results from classical geothermobarometry. Likewise, a value of $fO2 \sim 0.2$ was used derived from using Fe^{3+}/Fe^{2+} ratios calculated from atomic units per formula from the garnet major element analyses.

The *P-T* pseudosection was calculated with the Perple_X 6.7.1 toolbox operated on a Mac Os X using the 'HP02ver.dat' datafile (Connolly, 1990, 2005; Holland and Powell, 1998). While HP02ver.dat is not the most recent datafile, it is considered to be the best option in combination with 'solution_model.dat' because all solution models of interest for this study are included, which is not the case in more recent solutions and data files. To constrain the physiochemical data in the *P-T* range of interest, we adapted and simplified the solution model files provided with the Perple_X toolbox. Non-existing end members and those occurring only in small concentrations of certain solutions were removed from the solution space (i.e. set to "0" in the solution file). The "disordered" Jadeite-Diopside-Hedenbergite-CaTs solution file was used for cpx (Gasparik, 1985). A modified hybrid solution file for garnet was used (Engi and Wersin, 1987; Holland and Powell, 1998) as well as the plagioclase solution model (Newton et al., 1980; Newton and Haselton, 1981) and an amphibole model without K, Ti and Mn in solution (Dale et al., 2000). For more details on the modeling calculations see Sommer and Kröner (2013).

The *P-T* pseudosection was processed in the NCMAFS system with H_2O and CO_2 in excess (Fig. 4). The minerals grt, cpx, plagioclase, clinoamphibole, kyanite, quartz, coesite and stishovite were used for the Perple_X calculation. The mineral modes and modal abundances based on whole rock composition predicted by the *P-T* pseudosection were compared and cross-checked with the calculated mineral end members based on major element analyses and measured mineral abundances obtained from planimetry (Figs. 5 and A2a and b). This resulted in a bulk rock composition of: Na_2O: 4.06 wt%; MgO: 10.12 wt%; Al_2O_3: 19.50 wt%; SiO_2: 48.26 wt%; CaO: 11.96 wt%; FeO: 6.49 wt%; O_2: 0.2 wt% and X_{H2O}: 0.9. The computed peak metamorphic mineral paragenesis is cpx, grt and coesite (Fig. 4).

The high-pressure history is documented by the kyanite-out reaction corresponding to stages 3–4 in Fig. 4 at ~890 °C and ~5.8 GPa, with a matching X_{Prp} in grt of ~0.46, X_{Grs} of ~0.32 and X_{Alm} of ~0.22 (Fig. 5a and b). The matching ratios in cpx during the high-pressure stage are ~0.70 for the (Na + Mg + Al)/(Ca + Si) exchange vector, MGTS ~0.32, CATS ~0.30, $X_{Di} \sim 0.38$ and $X_{Jd} \sim 0.30$ (Figs. 5e and A2). The predicted modal abundances from the Perple_X calculation are ~48% grt, ~50% cpx and ~2% kyanite, which match exactly the results gained from planimetry (Fig. 5c, d, and f and Table 1).

The high temperature stage 5, documented in the kyanite-free eclogite sections, is determined at ~1380 °C and ~5.3 GPa with a corresponding X_{Prp} in grt between ~0.53 and ~0.57, $X_{Grs} \sim 0.13$ to ~0.19 and $X_{Alm} \sim 0.25$ to ~0.27 (Fig. 5a and b). The MGTS, CATS, X_{Di}, X_{Jd} and a combination of these exchange vectors were calculated to describe the mineral chemical variation of clinopyroxene along the computed *P-T* path. During the high temperature stage of the metamorphic history, the theoretical MGTS is ~0.37, CATS is ~0.34, X_{Di} is ~0.46, X_{Jd} is ~0.25 and the (Na + Mg + Al)/(Ca + Si) exchange vector is ~0.67 (Figs. 5e and A2). The predicted modal abundances from the Perple_X calculation are ~34% grt and ~66% cpx, which again match exactly the results gained from planimetry (Fig. 5c, d, and f and Table 1).

Calculated $X_{Prp,Grs,Alm}$ ratios show the same composition as the calculated mineral end member ratios from the major element analyses (Table 2a) with few exceptions. We believe the mismatches are due to some alteration in the rock and/or local chemical disequilibrium.

According to our observations combined with these computations, grt is formed between metamorphic stages 1 and 3 (Figs. 4 and 5c) and is consumed between stages 3 and 5 as well as during retrograde stages 6 and 7. In comparison, cpx is formed at all stages including stage 6.

The calculated volumetric proportions gained from planimetry for the kyanite-bearing section in RV1570 are ~48% garnet, ~50% clinopyroxene and ~2% kyanite and ~34% garnet and ~66% omphacite for the bimineralic part (Figs. 5c, d, and f and Tables 1, A2a, A4c and A4e). The calculated volumetric concentrations from Perple_X match exactly with our planimetric results through all stages of the *P-T* path (Fig. 5c and d).

4.2. Trace elements

Trace element analyses were grouped into typical compositions of grt and cpx in the kyanite-bearing and

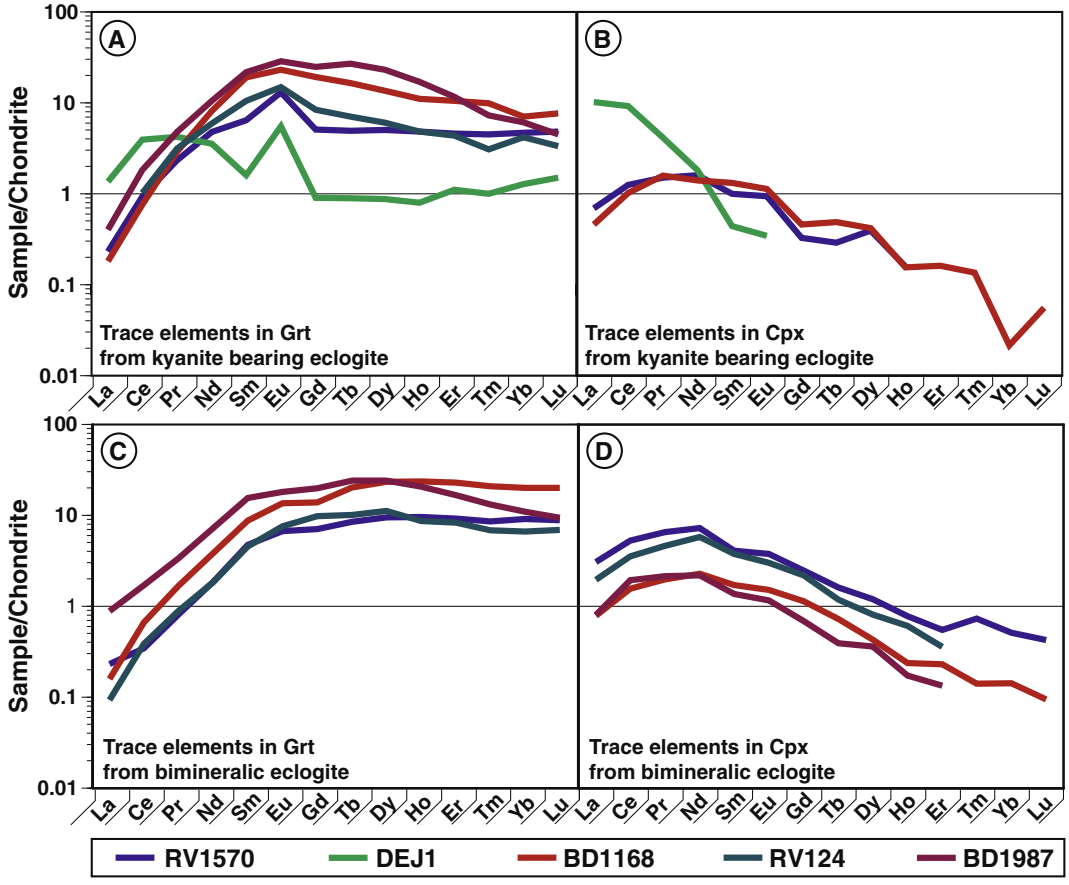

Fig. 6. Chondrite-normalized Rare Earth Element diagrams for garnets (A) and cpx (B) in kyanite-bearing sections as well as garnets (C) and cpx (D) in the bimineralic rock sections. Chondrite values are taken from Sun and McDonough (1989).

bimineralic sections of each sample (Table 3). Where possible, averages of several LA-ICPMS spot analyses were calculated.

Garnets from the kyanite-bearing parts of the samples all have prominent positive europium anomalies ($Eu^*_N = 1.21–4.40$) and flat or slightly declining Heavy Rare Earth Element (HREE) patterns (Fig. 6A). Light Rare Earth Elements (LREE) are depleted except for grts in DEJ1. Some garnets in DEJ1 display perhaps the most prominent positive Eu-anomalies of $Eu^*_N = 5.74$ yet observed in eclogite xenoliths. Coexisting cpx in the kyanite-bearing sections are often severely altered and could not be analyzed in every sample, but in some samples (DEJ1, RV1570, BD1168) clear cores were found. Their trace element contents are relatively low, up to ca. 10 times chondrite and many of the HREE are below detection limits of the LA-ICPMS (Fig. 6B and Table 3). BD1168 cpx has a positive Eu anomaly ($Eu^*_N = 1.28$) and DEJ1 cpx is distinctly LREE enriched.

Garnets in the bimineralic parts of the samples have negligible or only small positive Eu-anomalies ($Eu^*_N = 1.01–1.20$), relatively flat HREE patterns at around 10 times chondritic values with middle REE enrichment and depleted LREE hinging at Nd (Fig. 6C). Coexisting cpx have similar REE patterns to those cpx in the kyanite-bearing parts. Cpx in both petrographically different parts of the same samples (RV1570, BD1168) have higher overall REE content in the bimineralic part than in the kyanite-bearing part (Fig. 6D).

Garnets in the kyanite-bearing part of each sample are generally lower in High Field Strength Element (HFSE) concentrations (Table 3) than those in the bimineralic parts. They display more distinct troughs at Zr and Hf than in the bimineralic parts (Fig. 7A and B), while Zr/Hf ratios are generally higher, except for BD1987. Clinopyroxenes in the kyanite-bearing parts display similar trace element patterns at generally lower concentrations than those in the bimineralic parts of the samples (Fig. 7C and D). They also have slightly higher Zr/Hf ratios and higher positive Hf anomalies than the latter. As is typical for cpx, all have positive Sr anomalies except for cpx in DEJ1, which is strongly enriched in the LREE, thus disguising the characteristic Sr enrichment. Garnets and cpx in the kyanite-bearing parts are lower in Sc and V than their counterparts in the bimineralic parts (Table 3).

Bulk rock trace element compositions (Table 4) were calculated using the mineral abundances of grt and cpx given in Table 1. Trace element contributions from kyanite were not taken into account, because kyanite in mantle eclogites is typically very low in trace elements other than Ti, Cr and V (e.g. Aulbach et al., 2016), and hence has only a dilution effect on the general bulk trace element budget, which is accounted for by the modes in Table 1. Rutile was neglected as it is only present in BD1168 and

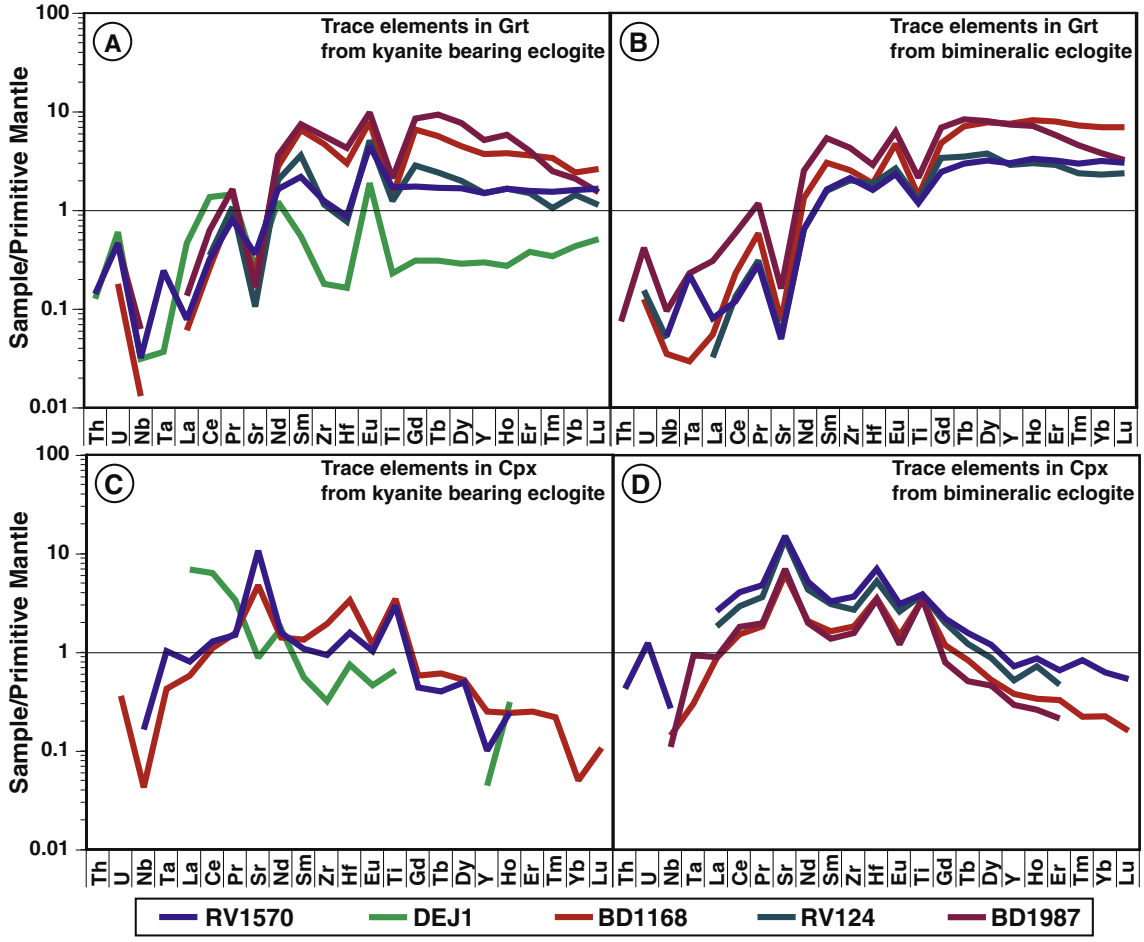

Fig. 7. Spidergrams normalized to values for primitive mantle (Sun and McDonough, 1989) for garnets (A) and cpx (C) in kyanite-bearing sections as well as garnets (B) and cpx (D) in the bimineralic rock sections.

BD1987 (Table 1) as immeasurably small grains; neither accurate modes of rutile nor trace element compositions could be obtained. Neglecting rutile only impacts on the budgets of the HFSE in BD1168 and BD1987, which are not essential for the discussion here. Note that RV1570 used for constructing the *P-T* path does not contain rutile. The recalculation method minimizes the effects of intergranular kimberlitic contamination, which distorts measured bulk rock trace element data. We estimate the uncertainty for the recalculated bulk rock trace element composition to be ~20% given the modal heterogeneity and large grain sizes of the samples. Calculated bulk rock spidergrams (Fig. 8) normalized to primitive mantle values (Sun and McDonough, 1989) are LREE depleted with prominent positive Sr- and Eu-anomalies and flat HREE patterns. The bimineralic section of BD1987 has the highest trace element concentrations, whereas the kyanite-bearing section of RV1570 is lowest in trace elements. For samples RV1570 and BD1168 for which bulk rock compositions for kyanite-bearing and kyanite-free parts could be calculated, the kyanite-bearing parts are always lower in overall trace element concentrations than the corresponding bimineralic parts. The kyanite-bearing sections in these two samples have higher normalized Zr/Hf values (RV1570 = 1, BD1168 = 1.2) than their bimineralic parts (RV1570 = 0.6, BD1168 = 1.0).

4.3. Oxygen isotopes

All samples show oxygen isotopic compositions (‰ $\delta^{18}O_{VSMOW}$) in garnet grains that are predominantly higher than the value of 5.5 ± 0.4‰ (Mattey et al., 1994) for average unaltered mantle (Fig. 9 and Table 5). Over the entire rock sections, $\delta^{18}O$ values in RV1570 garnets as measured by SIMS show the largest variability, between 5.3‰ and 6.6‰ (Table 5), BD1168 garnets range between 6.3‰ and 6.8‰, $\delta^{18}O$ values in RV124 garnets are between 6.1‰ and 6.6‰, while DEJ1 garnets are between 5.1‰ and 5.6‰. Garnets in RV1570 thus show a significant within-sample variation of 1.3‰, while the oxygen isotopic variation in all other samples is only 0.5‰ (Fig. 9). Garnets in the kyanite-bearing part of the sample with Ca-numbers >0.35 (Fig. 9) show the lowest $\delta^{18}O$ values, close to the mantle value (average 5.5‰), while those in the bimineralic part with Ca-numbers <0.35 (Fig. 9) are highest with an average of 6.1‰. In sample DEJ1 kyanites and overgrowth

Table 4
Calculated bulk trace element compositions using modal amounts from Table 1.

	RV1570	RV1570	BD1168	BD1168	RV124	DEJ1	BD1987
	ky	bi	ky	Bi	bi	ky	bi
Li	15.5	7.34	n.m.	n.m.	n.m.	n.m.	n.m.
Th	0.0052	0.0117	0.007	<0.001	<0.002	0.0160	0.003
U	0.0042	0.0056	0.003	0.001	0.001	0.004	0.004
Nb	0.0228	0.0417	0.006	0.023	0.031	0.033	0.0410
Ta	0.0116	0.0032	0.002	0.002	<0.01	0.001	0.0107
La	0.113	0.487	0.0676	0.105	0.266	1.45	0.200
Ce	0.663	2.15	0.489	0.652	1.29	3.91	1.11
Pr	0.174	0.428	0.191	0.173	0.281	0.349	0.262
Sr	73.7	128	23.1	30.3	101	4.91	39.9
Nd	1.37	2.47	2.00	1.47	1.87	1.00	12.21
Sm	0.504	0.660	1.39	0.852	0.30	0.116	1.29
Zr	7.79	20.1	27.4	19.0	16.9	1.12	26.9
Hf	0.210	0.892	0.617	0.531	0.686	0.0537	0.672
Eu	0.354	0.281	0.631	0.473	0.295	0.113	0.558
Ti	1827	1981	1673	1853	1948	230	2376
Gd	0.486	0.846	1.82	1.67	1.153	0.0592	2.10
Tb	0.0851	0.153	0.285	0.429	0.194	0.0159	0.457
Dy	0.588	1.03	1.55	3.20	1.35	0.0686	3.00
Y	2.97	5.51	7.77	19.0	6.19	0.449	16.91
Ho	0.123	0.222	0.286	0.740	0.238	0.0211	0.591
Er	0.326	0.607	0.794	2.09	0.649	0.0587	1.39
Tm	0.0538	0.0907	0.115	0.295	0.0783	0.008	0.167
Yb	0.342	0.614	0.541	1.89	0.520	0.0689	0.932
Lu	0.0583	0.0872	0.088	0.282	0.0788	0.0122	0.119
Cr	522	505	n.m.	n.m.	n.m.	n.m.	n.m.
Mn	755	1285	n.m.	n.m.	n.m.	n.m.	n.m.
Co	35.2	39.7	n.m.	n.m.	n.m.	n.m.	n.m.
Ni	206	228	n.m.	n.m.	n.m.	n.m.	n.m.
Zn	53.1	55.8	n.m.	n.m.	n.m.	n.m.	n.m.
V	107	215	83.2	158	136	31.5	156
Sc	20.35	22.32	18.2	29.5	19.7	8.68	18.5
P	56.0	98.5	n.m.	n.m.	n.m.	n.m.	n.m.

garnet pairs were measured *in situ* by SIMS. Kyanite and overgrowth garnet crystals are homogeneous within ca. 0.3‰ (Fig. A3), which corresponds roughly to within the analytical uncertainty; systematic core-rim relationships were not observed. Adjacent garnet-kyanite pairs have differences in $\delta^{18}O$ of 1.6–2.0‰.

The oxygen isotopic data obtained by SIMS compare very well with a dataset obtained by Laser-Fluorination Mass Spectrometry (LFMS, Table 5). LFMS data for cpx in BD 1168 yielded $\delta^{18}O = 7.2$‰ with a cpx-grt fractionation of 0.5‰, those in RV124 have $\delta^{18}O$ values of 6.6‰ (cpx-grt fractionation 0.3‰). Reversed fractionations were not observed. These fractionations are in the range of values observed for grt-cpx pairs in eclogite xenoliths observed in the literature (e.g. Jacob et al., 1994; Shu et al., 2016). Kyanites in BD1168 measured as mineral separates by LFMS are lighter in oxygen isotopes ($\delta^{18}O = 6.8$‰) than those in DEJ1 ($\delta^{18}O = 7.1$‰) and give a fractionation of ca. 0.2‰ between garnet and kyanite. The 2 sigma error for all analyzed garnets varies between 0.28 and 0.30 (Fig. 9 and Table 5).

The dataset was tested for linear correlations between $\delta^{18}O$-values and other geochemical parameters of garnet, particularly calcium concentrations, and Mg-number. None of these parameters showed a statistically robust correlation within the dataset.

4.4. Water content of kyanite

FTIR spectra of ten kyanite grains from RV1570 were measured in a doubly polished rock thick section of 248 μm thickness. The spectrum for kyanite (Fig. 10) shows four bands, namely a triplet at 3386, 3410 and 3440 cm^{-1} with normalized intensities ranging between 0.04 and 0.11 and a lower energy band at 3275 cm^{-1}. The Beer–Lambert law was used to calculate the water content from the FTIR spectra in all ten measured grains, with a molar absorption coefficient of 0.147 (Bell et al., 2004). The total absorbance of the fundamental OH stretching bands in the 3700–3050 cm^{-1} region and the areas underneath the OH peaks were integrated in all three directions (α, β, γ), then added up and normalized to 1. This resulted in an average calculated H_2O concentration in the kyanite grains of 97 ± 8 ppm (2 sigma), comparable to H_2O concentrations of 58–100 ppm in kyanite grains from the Roberts Victor mine from the literature (Beran and Götzinger, 1987; Rossman and Smyth, 1990; Wieczorek et al., 2004).

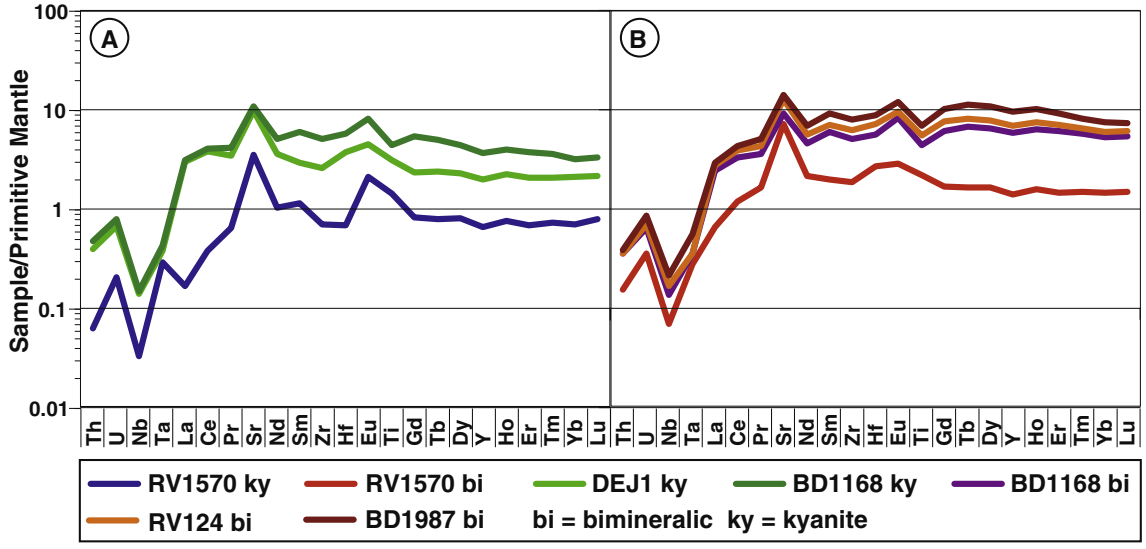

Fig. 8. Spidergrams normalized to values for primitive mantle (Sun and McDonough, 1989) for recalculated bulk rock compositions (Tables 1 and 4) for kyanite-bearing sections (A) and bimineralic parts (B) of the samples.

5. DISCUSSION

5.1. Origin of kyanite eclogites in the Earth's mantle

The eclogite xenolith suite at Roberts Victor was amongst the first suites of mantle eclogites for which an origin as subducted altered oceanic crust was proposed (MacGregor and Manton, 1986). This genetic interpretation was originally based on the widely varying oxygen isotopic composition of the eclogitic garnets, which cover a large range between 2.5‰ and 8‰ (MacGregor and Manton, 1986), analogous to the range found in oceanic crust and in ophiolites. Many more characteristics of these rocks have since been found to support their origin from the surface of the Earth. Kyanite, in particular, provides key evidence for a metamorphic origin of eclogite rocks from the surface of the Earth (Nixon et al., 1963), as this mineral is not in equilibrium with the peridotitic mantle nor can it be precipitated from high-pressure mantle melts. In mafic rocks, kyanite typically forms during prograde metamorphism upon breakdown of plagioclase and in the absence of fluids can be stable at mantle pressures and temperatures.

Many eclogite xenoliths from kimberlites contain quartz/coesite or are quartz normative, with bulk compositions rich in Al_2O_3 and high jadeite-component in omphacite (e.g., Shu et al., 2016). They have positive europium and strontium anomalies and flat HREE patterns which are similar to metagabbros and metabasalts (e.g. Jacob, 2004; Aulbach et al., 2016; Shu et al., 2016; Aulbach and Jacob, 2016). Frequently, however, the low-pressure prehistory of bimineralic eclogities can be disguised by an extensive and multi-stage history of mantle melting and metasomatism (Greau et al., 2011; Huang et al., 2012).

Positive Eu and Sr anomalies in the bulk rock are indicative of the existence of plagioclase in the magmatic precursors of eclogites (Jacob et al., 2003). Partition coefficients between basaltic mineral/melt pairs show that strong positive Eu anomalies develop when plagioclase crystallizes together with olivine, because Sr and Eu have greater compatibility in plagioclase compared to olivine or other miner-

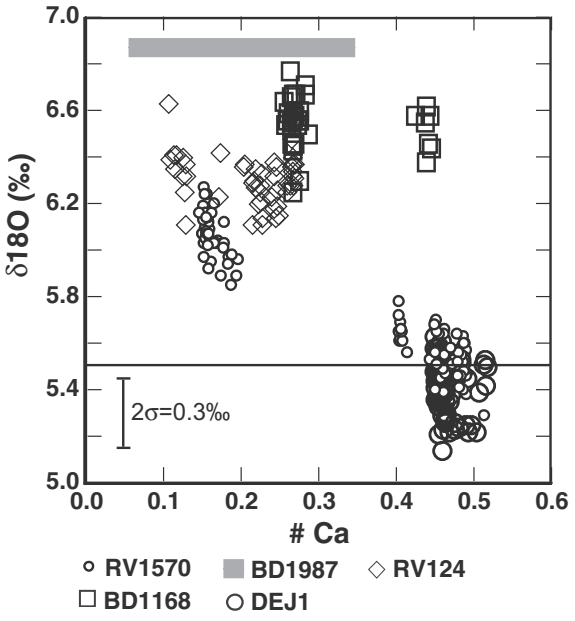

Fig. 9. Oxygen isotopic compositions of garnets plotted against their Ca-number (Ca# = Ca/(Ca + Mg + Fe)). Garnets with high Ca# coexist with kyanite. Uncertainties (2σ) range between 0.2‰ and 0.3‰ (see Table 3). High Ca-numbers, mostly > 0.35 occur in garnets in the kyanite-bearing parts of the samples, low Ca-numbers are those in bimineralic parts, plotting to the left. The gray bar for BD1987 shows the range of garnet Ca# in the sample and Laser Fluorination oxygen isotopic data on mineral separates. No correlated major element and oxygen isotope analyses exist for sample BD1987.

Table 5
Average oxygen isotopic composition in ‰ $\delta^{18}O_{VSMOW}$ for garnet, kyanite and clinopyroxene determined by SIMS or by Laser Fluorination Mass Spectrometry (LFMS). "part" denotes the paragenetic association in the kyanite-bearing part (ky), the reaction zone (react) or the bimineralic part (bi) of the samples.

	Part	n	$\delta^{18}O$	2σ	SD	%SD	min	max
RV1570 grt SIMS part (A)	bi	96	6.19	0.29	0.15	2.4	5.85	6.63
RV1570 grt SIMS part (B)	react	12	5.68	0.29	0.09	1.6	5.56	5.91
RV1570 grt SIMS part (C)	ky	54	5.54	0.29	0.09	1.6	5.29	5.7
BD1168 grt SIMS	ky	34	6.44	0.29	0.11	1.7	6.25	6.77
BD1168 grt LFMS	bi	6	6.70	0.3	0.11	1.6		
BD1168 cpx LFMS	bi	1	7.23	0.32				
BD 1168 ky LFMS	ky	2	6.80	0.33				
RV124 grt SIMS	'ky'	49	6.30	0.29	0.10	1.6	6.11	6.63
RV124 grt LFMS	bi	6	6.28	0.28	0.06	1.0		
RV124 cpx LFMS	bi	4	6.64	0.3	0.04	0.6		
DEJ1 grt SIMS	ky	94	5.42	0.28	0.11	2.0	5.14	5.63
DEJ1 ky SIMS	ky	102	7.12	0.21	0.11	1.5	6.86	7.38
BD1987 grt LFMS	ky	2	7.01	0.30	0.20	2.9	6.92	7.10
BD1987 grt LFMS	bi	2	6.77	0.30	0.20	2.9	6.64	6.77
BD1987 cpx LFMS	bi	6	7.21	0.33	0.08	1.1	7.07	7.30
BD1987 ky LFMS	ky	4	7.26	0.32	0.23	3.1	6.99	7.46

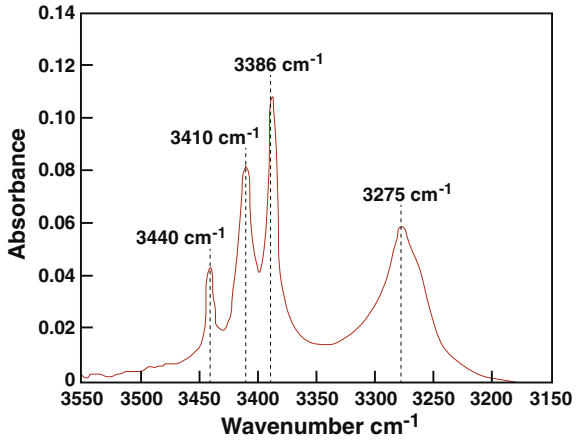

Fig. 10. FTIR spectrum of kyanite in RV 1570 (average of ten spectra) showing the typical triplet at 3386, 3410 and 3440 cm^{-1}.

als, by a factor of 50 (Drake and Weill, 1975; Paster et al., 1974; Fujimaki et al., 1984; Beattie, 1993, 1994; Bindeman et al., 1998). Hence, a considerable positive Sr anomaly can still be detected in bulk compositions with modal plagioclase abundances too low to cause positive Eu anomalies in the bulk rock (Schmickler et al., 2004).

CIPW norms for all samples studied here indicate an olivine gabbro as the magmatic precursor for the samples (Table 6). Hence the Roberts Victor kyanite eclogite samples in this study likely formed part of a metagabbroic-metabasaltic suite of former seawater-altered oceanic crust that resided at deeper lithospheric pressures, but lower temperatures since the Archaean (ca. 2.7 Ga; Jagoutz et al., 1984).

5.2. Subsolidus breakdown of kyanite

The kyanite-bearing parts of the layered samples studied here show clear evidence for a subsolidus breakdown reaction that forms garnet at the expense of kyanite (Fig. 2). The breakdown reaction of kyanite was first described by Lappin and Dawson (1975) in eclogite xenoliths from Roberts Victor as a reaction involving garnet and clinopyroxene forming a second generation of these minerals, with modal kyanite being partly or completely consumed:

$$\mathrm{Cpx}(1) \pm \mathrm{Grt}(1) \pm \mathrm{Ky} \rightarrow \mathrm{Cpx}(2) + \mathrm{Grt}(2) \pm \mathrm{Ky}$$

The extensive solid solution series of both garnet and cpx can easily accommodate the kyanite component, particularly as it is a small component with modal amounts between about 2 and ca. 20 vol% in this sample suite (Table 1). The kyanite-out reaction leads to a shift in the modal composition towards higher garnet modes in the samples as a consequence of the high Al concentrations in kyanite. Depending on the distribution of kyanite in the rock, the modes of garnet can be pushed locally to very high values, even as high as 90 vol% (Fig. 1).

The breakdown reaction of kyanite has a significant effect on the distribution of the major and trace elements: Newly formed garnets in the kyanite-free sections are notably more pyropic than their grossular-rich parents in the kyanite-bearing parts (Fig. 3A and B) and relict fassaitic cores are preserved in diopside-rich clinopyroxenes in the bimineralic parts in RV 1570 (Table 2c). The fassaitic cores are interpreted as the first reaction product (cpx_2) of the kyanite-out recation, overgrown by diopside formed during the high temperature event (Stage 5, see below).

In terms of trace element characteristics, the original garnets in the kyanite-bearing sections show prominent positive Eu anomalies and flat HREE patterns with Gd/Yb ratios between 0.5 and 1.5 (Fig. 11), whereas the reaction product garnets of the kyanite-out reaction in the bimineralic parts have lost their Eu-anomalies but have higher Gd/Yb of up to 4.5, attaining a more middle REE-enriched nature, with slightly more convex HREE patterns than their parent garnets (Fig. 6A and C).

Table 6
Calculated bulk rock major element compositions with CIPW norms for the kyanite-bearing sections using modal amounts from Table 1.

	RV1570	RV1570	BD1168	BD1168	RV124	RV124	DEJ1	BD1987	BD1987
	ky	bi	ky	bi	(ky)	bi	ky	ky	bi
SiO_2	49.24	50.37	47.04	47.38	42.23	49.56	48.24	45.68	48.24
TiO_2	0.34	0.33	0.23	0.24	0.28	0.33	b.d.l.	0.30	0.37
Al_2O_3	19.50	14.90	24.40	20.54	21.70	14.65	22.05	29.29	20.90
Cr_2O_3	b.d.l.	b.d.l.	b.d.l.	b.d.l.	b.d.l.	b.d.l.	b.d.l.	b.d.l.	b.d.l.
FeO	5.63	7.17	7.43	9.40	11.98	10.39	3.12	6.59	8.52
MnO	b.d.l.	b.d.l.	b.d.l.	b.d.l.	b.d.l.	0.27	b.d.l.	b.d.l.	b.d.l.
MgO	7.25	12.31	6.10	8.73	12.84	12.89	9.26	5.34	7.57
CaO	13.76	10.65	11.74	10.09	9.63	9.25	14.19	9.29	10.59
Na_2O	4.62	4.07	3.34	3.33	0.76	2.87	2.86	3.33	4.06
K_2O	b.d.l.	b.d.l.	b.d.l.	b.d.l.	b.d.l.	b.d.l.	b.d.l.	b.d.l.	b.d.l.
Total	100.32	99.80	100.27	99.71	99.42	100.19	99.89	99.82	100.23
plag	47.82	46.16	70.24	62.75	54.21	51.38	62.02	73.79	60.83
ne	12.86	5.78	5.19	3.54	2.94	–	5.15	0.26	6.68
cor	–	–	–	–	–	–	–	6.92	–
di	29.04	24.52	5.48	7.35	9.98	15.29	18.37	–	11.28
hy	–	–	–	–	–	4.15	–	–	–
ol	9.96	22.71	18.91	25.62	31.76	28.76	14.34	18.28	20.76
il	0.65	0.63	0.44	0.46	0.53	0.63	–	0.57	0.70

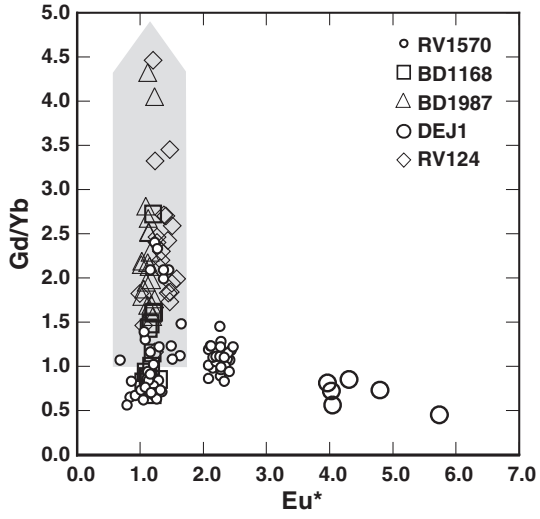

Fig. 11. Eu-anomaly ($Eu^* = (Eu/(Sm + Gd)/2)$ vs Gd/Yb ratio (as a measure of curvature of the HREE patterns) in garnets. Kyanite-bearing samples DEJ1 and RV1570 with $\delta^{18}O$ similar to unchanged mantle (Fig. 8) have highest Eu^* and lowest Gd/Yb, while bimineralic parts from which the kyanite has been reacted out have lost most of their excess Eu and display high Gd/Yb ratios.

A mass balance approach was used for RV1570 to illustrate the effects of the kyanite-out reaction in more detail. By minimizing the mass flux of all major element oxides (Figs. 12 and 13A, and A4; Tables A2a–A2d) it can be shown that 0.7 mol of Grs-rich garnet and 0.3 mol of cpx from the kyanite-bearing eclogite are required per mole of grt formed in the bimineralic part of the sample. Similarly, 1 mol of omphacite (cpx_2) in the bimineralic eclogite was formed by 0.725 mol of Na-rich omphacite and 0.275 mol of Grs-rich garnet from the kyanite-bearing part (Fig. 12).

Both partial reactions were balanced with each other according to molar proportions of grt and cpx formed in the bimineralic parts (Fig. 12). Finally, the reaction was balanced with kyanite, as well as with minor amounts of quartz/coesite, and calcite (Fig. A4). Quartz/coesite and calcite were not observed in the samples, but are inferred for balancing purposes. For the mass balance approach, the following atomic units were calculated and the total mean composition was standardized to Si = 1.

Grt_1 : Grossular-rich garnet

: $Ca_{0.50}Mg_{0.30}Fe_{0.22}Al_{0.64}Si_{1.0}O_{4.0}$

Cpx_1 : Ts-Na-rich omphacite

: $Na_{0.28}Ca_{0.21}Mg_{0.19}Fe_{0.03}Al_{0.32}Si_{1.0}O_{3.0}$

Grt_2 : Pyrope garnet : $Ca_{0.15}Mg_{0.58}Fe_{0.28}Al_{0.64}Si_{1.0}O_{4.0}$

Cpx_2 : Ca-rich omphacite

: $Na_{0.04}Ca_{0.51}Mg_{0.30}Fe_{0.14}Al_{0.50}Si_{1.0}O_{3.0}$

The standardized mean composition of the rock-forming minerals was normalized to the respective Si units of each mineral formula and the eclogite forming reaction was then balanced as:

$$0.975\ \text{Grs-rich garnet} + 1.025\ \text{Na-rich omphacite} + 0.15\ \text{kyanite} + 0.26\ \text{MgO} + 0.21\ \text{FeO} = 1\ \text{Pyp-rich garnet} + 1\ \text{Ca-rich omphacite} + 0.13\ Na_2O + 0.04\ \text{CaO}$$

This balanced reaction, based on the estimated mineral modes, is in good agreement with our theoretical pressure and temperature estimates in the pseudosection derived by Perple_X calculations. We interpret the addition of MgO and FeO and the removal of Na_2O and CaO (Figs. 13A and S4) as a result of restricted metasomatic influx. A mass balance carried out for the trace elements in sample RV1570 (Fig. 13B) takes into account the large uncertainty of ca. 20% in the modal estimates and shows

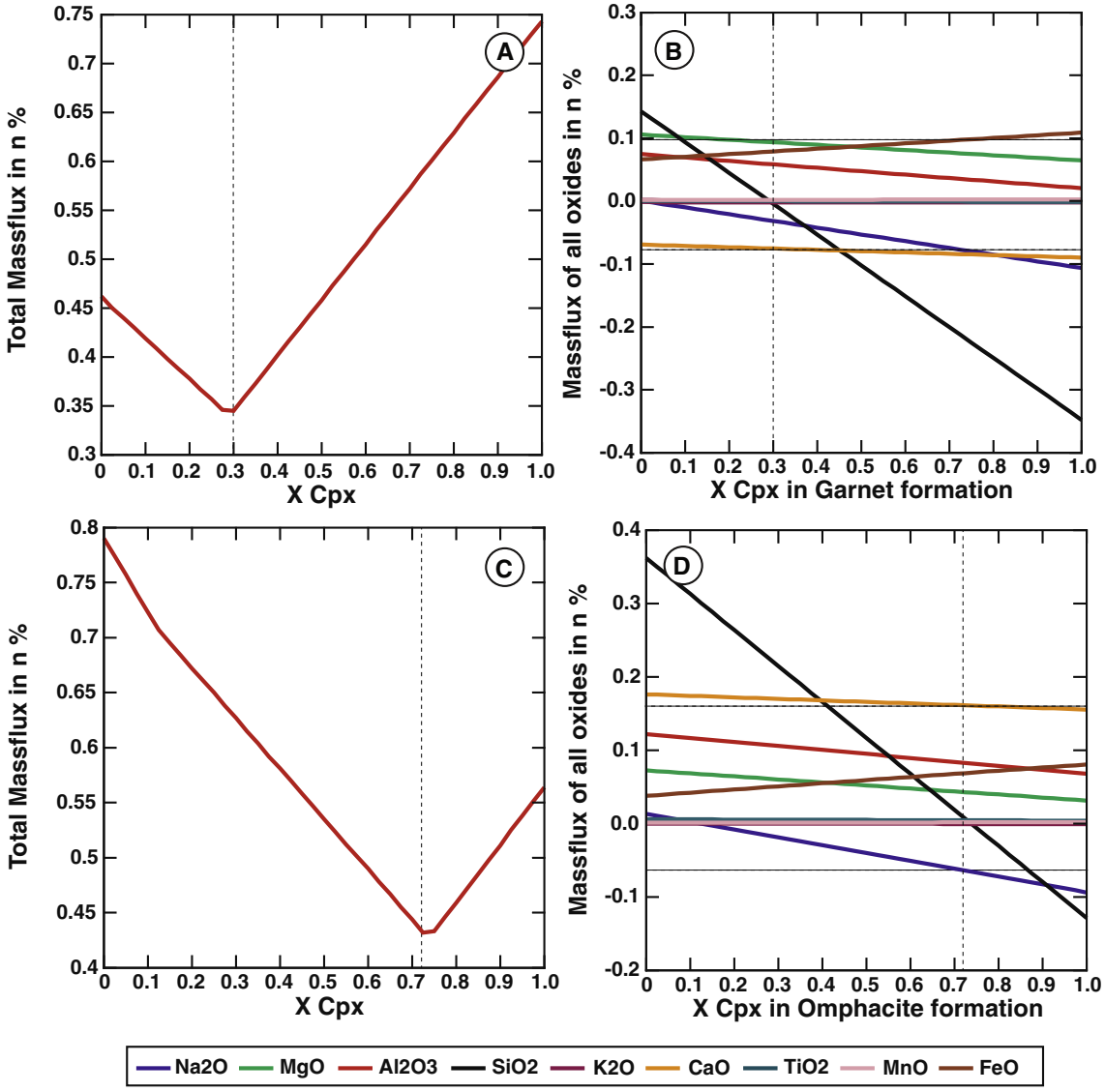

Fig. 12. (A) Total mass flux in% versus $X_{Cpx/ky\text{-}eclogite}$ for the garnet-forming reaction in bimineralic eclogite. (B) Total mass flux in% versus $X_{Cpx/Ky\text{-}eclogite}$ for the omphacite-forming reaction in bimineralic eclogite. (C) Mass flux of all elements in% versus $X_{Cpx/Ky\text{-}eclogite}$ for the garnet-forming reaction in bimineralic eclogite. (D) Mass flux of all elements in% versus $X_{Cpx/Ky\text{-}eclogite}$ for the omphacite-forming reaction in bimineralic eclogite.

loss of approximately 30% of the Eu component upon reaction from the kyanite-bearing to the bimineralic lithology. At the same time, addition of mainly Zr and Hf as well as of Th and LREE to the bimineralic paragenesis is recorded. The titanium content remains unchanged and HREE are slightly and uniformly increased in concentration in the bimineralic part compared to the kyanite-bearing assemblage (Fig. 13B).

5.3. Pressure-temperature path

Several geothermometers and/or -barometers exist for mantle eclogites (e.g. Ellis and Green, 1979; Simakov, 2008; Beyer et al., 2015). However, precise *P-T* path constructions for mantle xenoliths are very rare, because major constituent mineral phases in mantle rocks are limited and samples preserving both prograde and retrograde minerals are scarce. RV1570 represents a large and unusually inhomogeneous kyanite eclogite sample with some relict prograde and retrograde phases preserved in the rock. The chemical and petrographic inhomogeneity coupled with the existence of metastable phases in this sample, particularly the fassaitic cores in cpx, show that both metasomatic influx and melt loss must have been restricted. Therefore, an effort was made to characterize this rock in detail in order to explore the possibility of constructing a *P-T* path for kyanite-bearing eclogite xenoliths from the Roberts Victor kimberlite pipe.

From thermodynamic calculations, a 7 stage clockwise *P-T* path was constructed (Fig. 4). Stage (1) represents

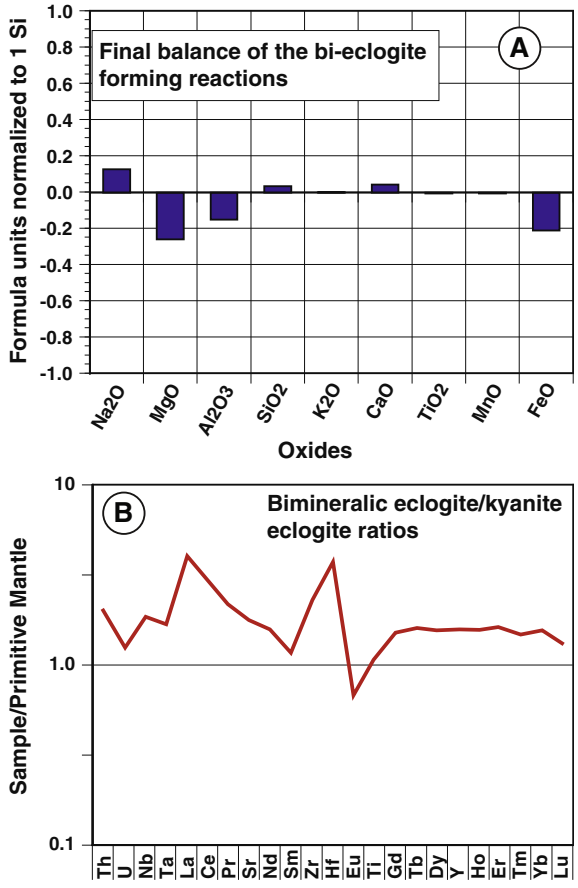

Fig. 13. (A) Net mass flux for major elements during formation of bimineralic eclogite from kyanite-bearing eclogite (see Fig. A4 for step-by-step mass balance calculation) and (B) trace element mass balance spidergram for primitive mantle normalized concentration ratios between kyanite-bearing and bimineralic eclogite. Primitive mantle values are taken from Sun and McDonough (1989).

the inferred transition from greenschist into blueschist at *P-T* conditions of ~480 °C and ~1.1 GPa (Figs. 4 and 5, A2a and b; Table A3a), in line with the metamorphic origin of this sample as an olivine gabbro. These *P-T* conditions are recorded in the most grossular-rich garnets and jadeite rich cpx ($X_{Pyp} = \sim 0.24$, $X_{Grs} = \sim 0.43$, $X_{Alm} = \sim 0.33$; MING = ~0.48, MGTS = ~0.10, CATS = ~0.10; Figs. 5a, b, and e and A2a and b; Tables A3 and A4a) in combination with the inferred plagioclase-out reaction to form kyanite in equilibrium with the analyzed grossular and jadeite pairs ($X_{An} = \sim 0.47$; Table A4a).

Stage (2) reflects the amphibole-out reaction. This stage is documented by the compositions of grossular-rich garnet and jadeite-rich cpx and the theoretical composition of amphibole in equilibrium ($X_{Mg} = \sim 0.96$; Table A3b) corresponding to these particular *P-T* conditions ($X_{Pyp} = \sim 0.46$, $X_{Grs} = \sim 0.26$, $X_{Alm} = \sim 0.28$; MING = ~0.66, MGTS = ~0.30, CATS = ~0.28; Figs. 5a, b, and e, and A2a and b; Tables A3 and A4b).

Stage (3) marks the beginning of the kyanite-out and the coesite-in reaction at 800 °C and 5.3 GPa, (Fig. 4). This stage is also documented by the chemical compositions of grt and cpx pairs ($X_{Pyp} = \sim 0.45$, $X_{Grs} = \sim 0.32$, $X_{Alm} = \sim 0.23$; MING = ~0.68, MGTS = ~0.29, CATS = ~0.29; Figs. 5a, b, and e and A2a and b; Tables A3 and A4c). Coesite is inferred but was not observed in the samples.

Stage (4) represents peak *HP* conditions at ~890 °C and ~5.8 GPa at a depth of ca. 190 km as well as the completion of the kyanite-out reaction in sample RV1570. This stage is documented by the chemical composition of grt and cpx pairs as well as by volumetric calculations ($X_{Pyp} = \sim 0.46$, $X_{Grs} = \sim 0.32$, $X_{Alm} = \sim 0.22$; MING = ~0.70, MGTS = ~0.32, CATS = ~0.31; Vol% Grt = ~48%, Vol % cpx = ~48%, Vol% Ky = ~2%, Figs. 4, 5, and A2a and b; Tables 1, A3, and A4d).

Stage (5) marks the peak *HT* conditions at ~1380 °C and ~5.3 GPa, coinciding with the Finsch geotherm (Bell et al., 2003; Mather et al., 2011) and the graphite/diamond transition curve (Day, 2012). These conditions are documented in the bimineralic sections of the sample using grt-cpx pairs and the volumetric calculations ($X_{Pyp} = \sim 0.55$, $X_{Grs} = \sim 0.16$, $X_{Alm} = \sim 0.29$; MING = ~0.67, MGTS = ~0.38, CATS = ~0.34; Volume (%) Grt = ~34%, Volume (%) cpx = ~66%, Figs. 4, 5, and A2a and b; Tables 1, A3, and A4e).

Stage (6) constrains the retrogression to conditions close to amphibolite/granulite facies. This is documented by the retrograde formation of amphibole and plagioclase found in the rock (Tables A2f and A3f).

Stage (7) documents sub-greenschist conditions at the Earth's surface indicated by late formation of natrolite (Table A3f and A4g).

5.4. Nature of the metasomatic agent and the role of kyanite

The kyanite-out reaction in eclogites has been previously described as a closed system reaction (Lappin and Dawson, 1975). However, our mass balance approach indicates that during the reaction from kyanite-bearing to bimineralic eclogite influx of major elements, namely ~20% MgO and FeO and ca. 10% loss of Na_2O is required (Figs. 13A and A4). Regarding the trace elements, the metasomatic agent introduced LREE, Th, Zr and Hf, while Eu was partly lost during the kyanite-out reaction (Fig. 13B). In part, the changes in trace element composition can be explained by changes in modal mineralogy and garnet crystal chemistry. They are consistent with trace element partitioning behavior in bimineralic eclogites (Harte and Kirkley, 1997) and are caused by crystal chemical changes due to the influence of the calcium ion (van Westrenen et al., 1999): Increasing grossular component in garnet leads to increasing compatibility of the middle REE and the HFSE, which enter both the eightfold *X* and the sixfold *Y* site in garnet in concert with increased Ca-concentration (van Westrenen et al., 1999, 2001).

Nevertheless, particularly the loss of ca. 30% of the Eu budget and the increases in Th, Zr, Hf and LREE (Fig. 13B), while most other trace elements remained relatively unaffected require some infiltration of the rock by a fluid or melt. A similar increase in these trace elements has been shown to occur as a result of the infiltration of peralka-

line melts in the Inagli dunite body in Siberia (Zinngrebe et al., 1995). Particularly an anomalous enrichment of Zr and Hf, while Ti remains unaffected, is associated with peralkaline melts with [Na + K]/Al > 1, as the mobilization of Zr occurs as Zr-Na-silicate complexes and depends on the degree of melt alkalinity (Watson and Harrison, 1983). The early reworking of the basal levels of subcratonic lithosphere during craton rejuvenation often results in the generation of peralkaline lamproitic melts, as in the first of three stages of magmatism that eventually led to the opening of the Labrador Sea (e.g. Tappe et al., 2007). High-pressure experiments have shown that the degree of peralkalinity is promoted by melting in reduced conditions (Foley, 1989), so that melts may be even perpotassic (K > Al). Thus, the anomalous increase in Zr and Hf could be caused by the solidification of, or reaction with, infiltrating peralkaline melts of lamproitic affinity, which are common during early phases of melting at the base of cratonic lithosphere.

At the same time, preservation of fassaitic relict cores in diopside and textural evidence for an incomplete and arrested kyanite-out reaction (Fig. 2) point to only a restricted role of metasomatism. Oxygen isotopes underpin this view. While each of the samples has its own characteristics in $\delta^{18}O$ that ranges between garnets with high Ca-numbers in the kyanite-bearing sections ((Ca/(Ca + Mg + Fe)) > 0.35; Fig. 9) and those with lower Ca-numbers in the bimineralic parts ((Ca/(Ca + Mg + Fe)) < 0.35; Fig. 9), there is no coherent trend across the sample population that links these two parts in their $\delta^{18}O$ systematics and hence *systematic* metasomatic over-printing of the oxygen isotope systematics has not occurred (see below).

Kyanites in mantle eclogites are of particular interest because of their elevated OH concentrations despite being nominally anhydrous (Beran and Götzinger, 1987; Rossman and Smyth, 1990; Beran et al., 1993). Hence, kyanite has the potential to carry significant amounts of water into the mantle upon subduction (Bell and Rossmann, 1992; Schmidt et al., 1998). The average OH concentration in kyanite from sample RV1570 is 97 ppm (Fig. 10), which is typical for kyanites from other Roberts Victor eclogites (58–100 ppm; Beran and Götzinger, 1987; Rossman and Smyth, 1990; Wieczorek et al., 2004).

Fig. 4 shows that kyanite reacts out along the *P-T* path at pressures and temperatures above ~800 °C and ~5.6 GPa in the mantle lithosphere in sample RV1570. Hence, we speculate that once the reaction was triggered and facilitated by heating and metasomatic infiltration, the release of water upon breakdown of kyanite in the eclogites catalyzed the kyanite-out reaction in these rocks.

5.5. Oxygen isotopes – subducted crustal signatures and a restricted role for mantle metasomatism

The sample suite shows variable oxygen isotopic characteristics for the kyanite-bearing sections (Fig. 9): Grossular-rich garnets coexisting with kyanite in samples DEJ1 and RV1570 have $\delta^{18}O$ values close or below to those of canonical Earth mantle values (5.5‰, Mattey et al., 1994), while BD1168 and BD1987 have significantly higher values at around 6.2–7‰ (Table 5). At the same time, DEJ1 and RV1570 (ky-part) have the most pronounced metagabbro signatures with strong positive Eu-anomalies and flat HREE patterns (Fig. 8) compared to BD1168 and BD1987.

This suggests that seawater alteration played a role for BD1168 and BD1987, but perhaps less so for DEJ1 and RV1570. It is well established that seawater alteration in the modern oceanic crust is closely correlated with structural weaknesses and porosity and therefore affects the rocks in a heterogeneous manner (Wilkens et al., 1991). Strongly altered and virtually unaffected lithologies can be found in close vicinity. Hence, the samples studied here, although lacking a uniform oxygen isotopic signal, could well have been part of the same section of oceanic crust.

The above conclusions are consistent with a long line of studies that have argued that Roberts Victor eclogite xenoliths represent the remnants of gabbroic oceanic crust that was altered by seawater prior to subduction and emplacement in the subcratonic lithosphere (e.g., MacGregor and Manton, 1986; Riches et al., 2016; Aulbach and Jacob, 2016). This hypothesis is based firmly on their large range of oxygen isotope compositions that vary between +2.5 and +8‰. In particular, the lower end of the range of $\delta^{18}O$ values <5.5‰ in the Group II eclogites cannot be generated at mantle depths. While the range ≥5.5‰ could potentially be explained by interaction of mantle-derived eclogites with metasomatic agents in the subcratonic lithosphere (Huang et al., 2012), the extreme fluid-rock ratios required for such alteration make this unlikely (Riches et al., 2016). Moreover, the layered rocks studied here do not show the correlated elemental and isotopic trends expected for such a process. In addition, oxygen isotope fractionation is insensitive to pressure (Clayton et al., 1975; Chacko et al., 2001). Thus, while metasomatic agents in the subcratonic lithosphere are theoretically able to alter, to limited extents, the oxygen isotopic composition of eclogites, the extreme nature of their isotopic range combined with a plethora of major and trace element signatures are best explained by low-pressure processes and cannot be generated in the Earth's mantle.

5.6. Geodynamic implications

The geochemical and P-T evolution of the Roberts Victor eclogite suite, particularly sample RV1570, have some interesting implications for craton formation. CIPW norm calculations show that the kyanite-bearing section of RV1570 was originally a troctolite or olivine gabbro, containing between 48 and 74 wt% plagioclase (Tables 6 and A3a). This observation is in agreement with the lower oceanic crustal protoliths proposed for aluminous eclogites from other localities in the Kaapvaal craton (Shu et al., 2016), highlighting the widespread nature of such recycled protoliths in the craton root. These rocks carry unambiguous surface signatures, such as kyanite, as well as oxygen isotopic and trace element systematics typical of oceanic metagabbros. Their widespread nature and *P-T*-t evolution can thus provide critical constraints on the evolution of cratonic roots.

The kyanite-out reaction is a clearly definable and probably late event in the evolution of banded eclogite RV1570.

This was most likely triggered by a heating event in the subcratonic lithosphere at conditions that changed between stage (4) at 5.8 GPa, and stage (5) at temperatures of 1380 °C (Fig. 4). We suggest that this reaction, once initiated, was accompanied by release of kyanite-hosted water, and may even have led to partial melting of rocks with high modal amounts of kyanite. The timing of this heating event in the Kaapvaal subcratonic lithosphere is unknown, mainly because it is very difficult to obtain isotopic ages for the kyanite-eclogites. The temperature of 1380 °C implied from mineral chemistry is close to or at the mantle isentrope and hence it could be speculated that this event occurred immediately prior to emplacement in the kimberlite. This, in turn, might be associated with the initiation of small-scale convective removal of the basal Kaapvaal lithospheric mantle (e.g., Bell et al., 2003; Mather et al., 2011), associated with the opening of the S. Atlantic ocean.

Of more fundamental importance in relation to the early *P-T* history of eclogites and what they reveal about craton-building processes relates to the earliest steps in the *P-T* path. Compared to a typical subduction geotherm, which defines a gradient of about 10 °C/km (Jaupart and Mareschal, 2011) the prograde *P-T* path for RV 1570 between stage (2) and stage (3) is very steep, with a "cold" gradient of 2 °C/km. Such a *P-T* path, with rapid compression accompanied by slow heating, might only be achieved by compressional thickening of the proto-cratonic lithosphere to form ~200 km thick cratonic mantle. Lateral compression has long been proposed as a mechanism for creating thick Archaean mantle lithosphere (Jordan, 1975; McKenzie and Priestley, 2008, 2016). Recent dynamical modeling by Wang et al. (in press) shows that initial tectonic shortening of previously depleted mantle can initiate the cratonization process. In this model, subsequent gravitational self-thickening contributes to a second thickening phase capable of building stable, thick cratonic roots that are robust to Rayleigh–Taylor type collapse. The *P-T* path documented by sample RV1570 may provide key evidence in support of such a mechanism.

To create thick depleted buoyant mantle lithosphere with remnants of gabbros as seen in this study, a depleted oceanic lithosphere is a pre-requisite, both for providing a viscous depleted layer for thickening and to create a layer of basaltic/gabbroid composition. Two scenarios appear to be possible: (1) Welding of the oceanic lithosphere into the overlying proto-cratonic lithosphere caused by flat buoyant subduction (Sommer, 2009), or (2) and more plausible given the colder *P-T* path required, is later compression associated with the closure of a pre-existing ocean along the N-S striking Colesberg lineament. We speculate that such steep, cold early *P-T* trajectories will be recovered from other cratonic eclogite xenoliths and that they will document a model of craton evolution that is dominated by compressional orogenic events (McKenzie and Priestley, 2016; Wang et al., in press). Density instabilities in the thickened lithospheric root may allow eclogites to re-distribute themselves through the lithospheric mantle, with some being lost into the convecting mantle (e.g., Pysklywec et al., 2010).

6. CONCLUSIONS

We show that kyanite eclogites offer a wealth of information not easily accessed via study of the more typical bimineralic eclogites. In particular, rare examples of samples that preserve, in composite form, zones of the original kyanite-bearing lithologies nested within kyanite-free lithologies, offer a unique view of the *P-T* evolution of these rocks throughout their complex history. The layered nature and reaction relationship between kyanite-bearing and bimineralic parts of some Roberts Victor eclogite xenoliths suggest that the aluminous zones may represent the original high pressure eclogites formed after subduction of broadly gabbroic oceanic crustal parental rocks. Kyanite subsequently reacts out during lithospheric heating to form the more common bimineralic garnet-cpx lithology seen in many cratons, with locally high garnet modes. This relatively diverse mineral assemblage allows, for the first time, the construction of a *P-T* path for mantle elcogites. The very high dP/dT transport gradient implied from the *P-T* path is difficult to reconcile with a simple subduction scenario and seems more consistent with compressional thickening – a mechanism previously invoked for craton formation.

Large, layered kyanite eclogites with a preserved, arrested kyanite–out reaction appear to be unique to Roberts Victor, but eclogitic mantle xenoliths with petrographic evidence for resorption of kyanite are also known from other localities (e.g. Dongre et al., 2015). The occurrence of kyanite in eclogitic mantle xenoliths is in line with their proposed origin as subducted oceanic crust, because gabbroic rocks are a volumetrically major part of the oceanic crust and kyanite is a common prograde metamorphic product of plagioclase-bearing mafic rocks. The preservation of the arrested kyanite-out reaction in mantle eclogites probably depends on the amount of metasomatic influx to facilitate the reaction, and thus on the local cratonic geodynamic evolution. In the absence of kyanite, very grossular rich garnets with positive Eu anomalies and anomalously high garnet modes in bimineralic mantle eclogites are indicators for plagioclase-bearing protoliths, providing strong evidence that bimineralic lithologies are products of a kyanite-out reaction that went to completion (e.g. Jacob et al., 1994; Pernet-Fisher et al., 2014). Compositional changes accompanying the metasomatically catalyzed kyanite-out reaction affect major and trace elements as well as isotopic systematics and most likely provide an explanation for the often erroneous radiogenic isotope cpx-garnet mineral ages in bimineralic mantle eclogites (e.g. Snyder et al., 1997). An important geochemical implication from this study is that mantle eclogites that originate from subducted gabbroic oceanic crust have a long metamorphic history accompanied by compositional changes that should not be neglected in reconstructing their origins.

ACKNOWLEDGEMENTS

We are grateful to the owner of the Roberts Victor Diamond mine for providing the sample RV1570. We thank the staff at the Department of Geosciences, University of Mainz, for assistance

during Laser ICPMS analysis and Nora Groschopf, Department of Geosciences, University of Mainz, for assistance during microprobe analyses. Comments from three anonymous reviewers helped to shape the ideas presented in this MS. The Canada Excellence Research Chairs program partly funded the analytical program. This is a contribution to IGCP-Project 557 and contribution 905 from the ARC Centre of Excellence for Core to Crust Fluid Systems (http://www.ccfs.mq.edu.au).

APPENDIX A. SUPPLEMENTARY MATERIAL

Supplementary data associated with this article can be found, in the online version, at http://dx.doi.org/10.1016/j.gca.2017.03.017.

REFERENCES

Aulbach S., Gerdes A. and Viljoen K. S. (2016) Formation of diamondiferous kyanite-eclogite in a subduction melange. *Geochim. Cosmochim. Acta* **179**, 156–176.

Aulbach S. and Jacob D. E. (2016) Major- and trace-elements in cratonic mantle eclogites and pyroxenites reveal heterogeneous sources and metamorphic processing of low-pressure protoliths. *Lithos* **262**, 586–605.

Aulbach S. and Viljoen K. S. (2015) Eclogite xenoliths from the Lace kimberlite, Kaapvaal craton: from convecting mantle source to palaeo-ocean floor and back. *Earth Planet. Sci. Lett.* **431**, 274–286.

Armstrong J. F. (1995) CITZAF: a package of correction programs for the quantitative electron microbeam X-ray analysis of thick polished materials, thin films, and particles. *Microbeam Anal.* **4**, 177–200.

Barth M., Rudnick R. L., Horn I., McDonough W. F., Spicuzza M., Valley J. W. and Haggerty S. E. (2001) Geochemistry of xenolithic eclogites from West Africa: part I. A link between low MgO eclogites and Archean crust formation. *Geochim. Cosmochim. Acta* **65**, 1499–1527.

Barth M. G., Rudnick R. L., Horn I., McDonough W. F., Spicuzza M., Valley J. R. and Haggerty S. E. (2002) Geochemistry of xenolithic eclogites from West Africa: part II. Origins of the high MgO eclogites. *Geochim. Cosmochim. Acta* **66**, 4325–4345.

Beattie P. (1993) Olivine-melt and orthopyroxene-melt equilibria. *Contrib. Miner. Petrol.* **115**, 103–111.

Beattie P. (1994) Systematics and energetics of trace element partitioning between olivine and silicate melt: implications for the nature of mineral/melt partitioning. *Chem. Geol.* **117**, 57–71.

Bell D. R. and Rossmann G. R. (1992) The distribution of hydroxyl in garnets from the subcontinental mantle of southern Africa. *Contrib. Mineral. Petrol.* **111**, 161–178.

Bell D. R., Schmitz M. D. and Janney E. (2003) Mesozoic thermal evolution of the southern African mantle lithosphere. *Lithos* **71**, 273–287.

Bell D. R., Rossman G. R., Maldener J., Endisch D. and Rauch F. (2004) Hydroxide in kyanite: a quantitative determination of the absolute amount and calibration of the IR spectrum. *Am. Mineral.* **89**, 998–1003.

Beran A. and Götzinger M. A. (1987) The quantitative IR spectroscopic determination of structural OH groups in kyanites. *Mineral. Petrol.* **36**, 41–49.

Beran A., Langer K. and Andrut M. (1993) Single crystal infrared spectra in the range of OH fundamentals of paragenetic garnet, omphacite and kyanite in an eklogitic mantle xenolith. *Mineral. Petrol.* **48**, 257–268.

Beyer C., Frost D. J. and Miyajima N. (2015) Experimental calibration of a garnet-clinopyroxene geobarometer for mantle eclogites. *Contrib. Miner. Petrol.* **169**, 1–21.

Bindeman I. N., Davis A. M. and Drake M. J. (1998) Ion microprobe study of plagioclase-basalt partition experiments at natural concentration levels of trace elements. *Geochim. Cosmochim. Acta* **62**, 1175–1193.

Bloxam T. W. and Allen J. B. (1960) Glaucophane-schist, Eclogite, and Associated Rocks from Knockormal in the Girvan-Ballantrae Complex, South Ayrshire. *Trans. R. Soc. Edinburgh* **64**, 1–27.

Chacko T., Cole D. R. and Horita J. (2001) Equilibirum oxygen, hydrogen and carbon isotope fractionation factors applicable to geologic systems. In *Reviews in Mineralogy and Geochmistry 'Stable Isotope Geochemistry'*, vol. 43 (eds. J. W. Valley and D. R. Cole). Mineralogical Society of America, pp. 1–82.

Clayton R. N., Goldsmith J. R., Karel V. J., Mayeda T. K. and Newton R. C. (1975) Limits on the effect of pressure on isotopic fractionation. *Geochim. Cosmochim. Acta* **39**, 1197–1201.

Connolly J. A. D. (1990) Multivariable phase-diagrams – an algorithm based on generalized thermodynamics. *Am. J. Sci.* **290**, 666–718.

Connolly J. A. D. (2005) Computation of phase equilibria by linear programming: a tool for geodynamic modeling and its application to subduction zone decarbonation. *Earth Planet. Sci. Lett.* **236**, 524–541.

Dale J., Powell R., White R. W., Elmer F. L. and Holland T. J. B. (2000) A thermodynamic model for Ca–Na clinoamphiboles in Na_2O - CaO - FeO – MgO - Al_2O_3 - SiO_2 - H_2O - O for petrological calculations. *J. Metamor. Geol.* **23**, 771–791.

Day H. W. (2012) A revised diamond-graphite transition curve. *Am. Mineral.* **97**, 52–62.

Dongre A. N., Jacob D. E. and Stern R. (2015) Subduction-related origin of eclogite xenoliths from the Wajrakarur kimberlite field, Eastern Dharwar craton, Southern India: constraints from petrology and geochemistry. *Geochim. Cosmochim. Acta* **166**, 165–188.

Drake M. and Weill D. (1975) Partition of Sr, Ba, Ca, Y, Eu^{2+}, Eu^{3+} and other REE between plagioclase feldspar and magmatic liquid: an experimental study. *Geochim. Cosmochim. Acta* **39**, 689–712.

Engi M. and Wersin P. (1987) Derivation and application of a solution model for calcic garnet. *Schweiz. Mineral. Petrograph. Mitt.* **67**, 53–73.

Ellis D. J. and Green D. H. (1979) An experimental study of the effect of Ca upon garnet-clinopyroxene Fe-Mg exchange equilibria. *Contrib. Mineral. Petrol.* **71**, 13–22.

Field M. J., Stiefenhofer J., Robey J. and Kurszlaukis S. (2008) Kimberlite-hosted diamond deposits of southern Africa: a review. *Ore Geol. Rev.* **34**, 33–75.

Foley S. F. (1989) Experimental constraints on phlogopite chemistry in lamproites: 1. The effect of water activity and oxygen fugacity. *Euro. J. Mineral.* **1**, 411–426.

Fujimaki H., Tatsumoto M. and Aoki K. (1984) Partition coefficients of Hf, Zr and REE between phenocrysts and groundmasses. In *Proceedings of the 14th Lunar Planetary Science Conference*, vol. 89, pp. B662–B672. J. Geophys. Res. (supplement).

Gasparik T. (1985) Experimentally determined compositions of diopside-jadeite pyroxene in equilibrium with albite and quartz at 1200–1350 °C and 15–34 kbar. *Geochim. Cosmochim. Acta* **49**, 865–870.

Greau Y., Huang J. X., Griffin W. L., Renac C., Alard O. and O'Reilly S. Y. (2011) Type I eclogites from Roberts Victor kimberlites: products of extensive mantle metasomatism. *Geochim. Cosmochim. Acta* **75**, 6927–6954.

Griffin W. L., Powell W. J., Pearson N. J. and O'Reilly S. Y. (2008) GLITTER: data reduction software for laser ablation ICP-MS (appendix). In *Laser Ablation-ICP-MS in the Earth Sciences*, vol. 40 (ed. P. Sylvester), pp. 308–311. Short Course Series. Mineralogical Association of Canada (MAC).

Harte B. and Kirkley M. B. (1997) Partitioning of trace elements between clinopyroxene and garnet: data from mantle eclogites. *Chem. Geol.* **136**, 1–24.

Holland T. J. B. and Powell R. (1998) An internally consistent thermodynamic data set for phases of petrological interest. *J. Metamor. Geol.* **16**, 309–343.

Huang J. X., Greau Y., Griffin W. L., O'Reilly S. Y. and Pearson N. J. (2012) Multi-stage origin of Roberts Victor eclogites: progressive metasomatism and its isotopic effects. *Lithos* **142**, 161–181.

Ickert R. B. and Stern R. A. (2013) Matrix corrections and error analysis in high-precision SIMS 18 O/16 O measurements of Ca-Mg-Fe garnet. *Geostand. Geoanal. Res.* **37**(4), 429–448. http://dx.doi.org/10.1111/j.1751-908X.2013.00222.x.

Ireland T. R., Rudnick R. L. and Spetsius Z. (1994) Trace elements in diamond inclusions from eclogites reveal link to Archean granites. *Earth Planet. Sci. Lett.* **128**, 199–213.

Jacob D., Jagoutz E., Lowry D., Mattey D. and Kudrjavtseva G. (1994) Diamondiferous eclogites from Siberia: remnants of Archean oceanic crust. *Geochim. Cosmochim. Acta* **58**, 5191–5207.

Jacob D., Jagoutz E., 1994. A diamond -graphite bearing eclogite xenolith from the Roberts Victor (South Africa): indications for petrogenesis from Pb-, Nd- and Sr isotopes. In: Meyer, H.O.A., Leonardos, O.H. (Eds.), Kimberlites, Related Rocks and Mantle Xenoliths. Proceedings of the Fifth International Kimberlite Conference. Companhia de Pesquisa de Recursos Minerais Special Publication 1B Jan/94, Araxa, Brasi, pp. 304–317.

Jacob D. E., Jagoutz E., Lowry D. and Zinngrebe E. (1998) Comment on "The Origins of Yakutian Eclogite Xenoliths" by G.A. Snyder, L.A. Taylor, G. Crozaz, A.N. Halliday, B.L. Beard, V.N. Sobolev and N.V. *Sobolev. J. Petrol.* **39**, 1527–1533.

Jacob D. E. and Foley S. F. (1999) Evidence for Archean ocean crust with low high field strength element signature from diamondiferous eclogite xenolith. *Lithos* **48**, 317–336.

Jacob D. E., Schmickler B. and Schulze D. J. (2003) Trace element geochemistry of coesite-bearing eclogites from the Roberts Victor kimberlite, Kaapvaal craton. *Lithos* **71**, 337–351.

Jacob D. E. (2004) Nature and origin of eclogites from the Earth's mantle. *Lithos* **77**, 295–316.

Jacob D. E. (2006) High sensitivity analysis of trace element-poor geological reference glasses by laser ablation-inductively coupled plasma-mass spectrometry (LA-ICP-MS). *Geostand. Geoanal. Res.* **30**, 221–235.

Jagoutz, E., Dawson, J.B., Hoernes, S., Spettel, B., Wänke, H., 1984. Anorthositic oceanic crust in the Archean Earth. In: 15th Lunar Planetary Science Conference, pp. 395–396 (Abs.).

Jaupart C. and Mareschal J. C. (2011) *Heat Generation and Transport in the Earth*. Cambridge University Press, p. 464.

Jochum, K, P., Nehring, F., 2006. GeoReM Preferred Values <http://georem.mpch-mainz.gwdg.de/>.

Jordan T. H. (1975) The continental tectosphere. Reviews. *Geophysics* **13**, 1–12.

Lappin M. A. and Dawson J. B. (1975) Two Roberts Victor cumulate eclogites and their reequilibration. *Phys. Chem. Earth* **9**, 351–366.

MacGregor I. D. and Carter J. L. (1970) The chemistry of clinopyroxenes and garnets of eclogite and peridotite xenoliths from the Roberts Victor Mine, South Africa. *Phys. Earth Planet. Inter.* **3**, 391–397.

MacGregor I. D. and Manton W. I. (1986) Roberts Victor eclogites: ancient oceanic crust. *J. Geophys. Res.* **91**(B14), 14063–14079.

Mather K. A., Pearson D. G., McKenzie D., Kjarsgaard B. and Priestley K. (2011) Constraining the depth and thermal history of cratonic lithosphere using peridotite xenolith and xenocryst thermobarometry and seismology. *Lithos* **125**, 729–742.

Mattey D. P. and MacPherson C. G. (1993) High-precision oxygen isotope microanalysis of ferromagnesian minerals by laser-fluorination. *Chem. Geol.* **105**, 305–318.

Mattey D., Lowry D. and MacPherson C. (1994) Oxygen isotope composition of mantle peridotite. *Earth Planet. Sci. Lett.* **128**, 231–241.

McCandless, T.E., Gurney, J.J., 1989. Sodium in garnet and potassium in clinopyroxene; criteria for classifying mantle eclogites. In: Ross, J., Jaques, A.L., Ferguson, J., Green, D. H., O'Reilly, S.Y., Danchin, R.V., Janse, A.J.A. (Eds.), Kimberlites and Related Rocks. Special Publication—Geological Society of Australia, vol. 14, pp. 827–832 (Perth).

McKenzie D. P. and Priestley K. (2008) The influence of lithospheric thickness variations on continental evolution. *Lithos* **102**, 1–11.

McKenzie D. P. and Priestley K. (2016) Speculations on the formation of crtaons and cratonic basins. *Earth Planet. Sci. Lett.* **435**, 94–104.

Morimoto N., Fabries J. and Ferguson A. K. (1988) Nomenclature of pyroxenes. *Am. Mineral.* **73**, 1123–1133.

Newton R. C., Charlu T. V. and Kleppa O. J. (1980) Thermochemistry of the high structural state plagioclases. *Geochim. Cosmochim. Acta* **44**, 933–941.

Newton R. C. and Haselton H. T. (1981) Thermodynamics of the garnet-plagioclase-Al_2SiO_5 quartz geobarometer. In *Thermodynamics of Minerals and Melts* (eds. R. C. Newton, A. Navrotsky and B. J. Wood). Springer, New York, pp. 129–145.

Nikitina L. P., Koroleva N. M., Zinchenko V. N. and Tunga Felix J. (2014) Eclogites from the upper mantle beneath the Kasai Craton (WesternAfrica): petrography, whole-rock geochemistry and U Pb zircon age. *Precamb. Res.* **249**, 13–32.

Nixon P. H., Knorring O. V. and Rooke J. M. (1963) Kimberlites and associated inclusions in Basutoland: a mineralogical and geochemical study. *Am. Mineral.* **48**, 1090–1132.

Paster H., Schauwecker D. S. and Haskin L. A. (1974) The behavior of some trace elements during solidification of the Skaergaard layered series. *Geochim. Cosmochim. Acta* **38**, 1549–1577.

Pearson D. G., Snyder G. A., Shirey S. B., Taylor L. A., Carlson R. W. and Sobolev N. V. (1995) Archean Re–Os age for Siberian eclogites and constraints on Archean tectonics. *Nature* **374**, 711–713.

Pernet-Fisher J. F., Howarth G. H., Liu Y., Barry P. H., Carmody L., Valley J. W., Bodnar R. J., Spetsius Z. V. and Taylor L. A. (2014) Komsomolskaya diamondiferous eclogites: evidence for oceanic crustal protoliths. *Contrib. Miner. Petrol.* **167**, 1–17.

Pysklywec R. N., Gogus O., Percival J., Cruden A. R. and Beamont C. (2010) Insights from geodynamic modeling on possible fates of continental mantle lithosphere: collision, removal and overturn. *Can. J. Earth Sci.* **47**, 541–563.

Rapp R. P., Shimizu N. and Norman M. D. (2003) Growth of early continental crust by partial melting of eclogite. *Nature* **425**, 605–609.

Riches A. J. V., Ickert R. B., Pearson D. G., Stern R. A., Jackson S. E., Ishikawa A., Kjarsgaard B. A. and Gurney J. J. (2016) In situ oxygen-isotope, major-, and trace-element constraints on the metasomatic modification and crustal origin of a diamondiferous eclogite from Roberts Victor, Kaapvaal Craton. *Geochim. Cosmochim. Acta.* **174**, 345–359.

Rusband, W., 2009. ImageJ 1.49v. National Institute of Health, USA.

Rollinson H. (1997) Eclogite xenoliths in West African kimberlites as residues from Archean granitoid crust formation. *Nature* **389**, 173–176.

Rossman G. R. and Smyth J. R. (1990) Hydroxyl contents of accessory minerals in mantle eclogites and related rocks. *Am. Mineral.* **75**, 775–780.

Schulze D. J. (1989) Constraints on the abundance of eclogite in the upper mantle. *J. Geophys. Res.* **94**(B4), 4205–4212.

Schmidt M. W., Finger L. W., Angel R. J. and Dinnebier R. E. (1998) Synthesis, crystal structure, and phase relations of AlSiO3OH, a high-pressure hydrous phase. *Am. Mineral.* **83**, 881–888.

Schmickler B., Jacob D. E. and Foley S. F. (2004) Eclogite xenoliths from the Kuruman kimberlites, South Africa: geochemical fingerprinting of deep subduction and cumulate processes. *Lithos* **75**, 173–207.

Sharp Z. D., Essene E. J. and Smyth J. R. (1992) Ultra-high temperatures from oxygen isotope thermometry of a coesite-sanidine grospydite. *Contrib. Mineral. Petrol.* **112**(2–3), 358–370. http://dx.doi.org/10.1007/BF00310466.

Shervais J. W., Taylor L. A., Lugmair G. W., Clayton R. N., Mayeda T. K. and Korotev R. L. (1988) Early Proterozoic oceanic crust and the evolution of subcontinental mantle: eclogites and related rocks from southern Africa. *Geol. Soc. Am. Bull.* **100**, 411–423.

Shirey S. B., Carlson R. W., Richardson S. H., Menzies A. H., Gurney J. J., Pearson D. G., Harris J. W. and Wiechert U. (2001) Archean emplacement of eclogitic components into the lithospheric mantle during formation of the Kaapvaal Craton. *Geophys. Res. Lett.* **28**, 2509–2512.

Shu Q., Brey G. P., Hoefer H. E., Zhao Z. and Pearson D. G. (2016) Kyanite/corundum eclogites from the Kaapvaal Craton: subducted troctolites and layered gabbros from the Mid- to Early Archean. *Contrib. Mineral. Petrol.* **171**, 11.

Silver P. G., Fouch M. J., Gao S. S. and Schmitz M.Kaapvaal Seismic Group (2004) Seismic anisotropy, mantle fabric, and the magmatic evolution of Precambrian southern Africa. *South African J. Geol.* **107**, 45–58.

Simakov S. K. (2008) Garnet–clinopyroxene and clinopyroxene geothermobarometry of deep mantle and crust eclogites and peridotites. *Lithos* **106**, 125–136.

Smit K. V., Stachel T., Creaser R. A., Ickert R. B., Dufrane S. A., Stern R. A. and Seller M. (2014) Origin of eclogite and pyroxenite xenoliths from the Victor kimberlite, Canada, and implications for Superior craton formation. *Geochim. Cosmochim. Acta* **125**, 308–337.

Smith C. B., Allsopp H. L., Kramers J. D., Hutchinson G. and Roddick J. C. (1985) Emplacement ages of Jurassic-Cretaceous South African kimberlites by the Rb–Sr method on phlogopite and whole-rock samples. *Trans. Geol. Soc. South Africa* **88**, 249–266.

Smyth J. R. and Hatton C. J. (1977) A coesite-sanidine grospydite from the Roberts Victor kimberlite. *Earth Planet. Sci. Lett.* **34**, 284–290.

Snyder G. A., Taylor L. A., Crozaz G., Halliday A. N., Beard B. L., Sobolev V. N. and Sobolev N. V. (1997) The origins of Yakutian eclogite xenoliths. *J. Petrol.* **38**, 85–113.

Sobolev N. V. (1977) *Deep-Seated Inclusions in Kimberlites and the Problem of the Composition of the Upper Mantle*. American Geophysical Union, Washington, DC, p. 279.

Sommer H. (2009) "Wet" low angle subduction: a possible mechanism below the Tanzania craton 2 Ga ago. *Mineral. Petrol.* **96**, 113–120.

Sommer H. and Kröner A. (2013) Ultra-high temperature granulite-facies metamorphic rocks from the Mozambique belt of SW Tanzania. *Lithos* **170–171**, 117–143.

Sun S.-S. and McDonough W. F. (1989) Chemical and isotopic systematics of oceanic basalts: implications for mantle composition and processes. In *Magmatism in the Ocean Basins*, vol. 42 (eds. A. D. Saunders and M. J. Norry). Geol Soc Spec Publ, pp. 313–345.

Tappe S., Foley S. F., Stracke A., Romer R. L., Heaman L. M., Kjarsgaard B. A. and Joyce N. (2007) Craton reactivation on the Labrador Sea margins: $^{40}Ar/^{39}Ar$ age and Sr-Nd-Hf-Pb isotope constraints from alkaline and carbonatite intrusives. *Earth Planet. Sci. Lett.* **256**, 433–454.

Tappe S., Smart K. A., Pearson D. G., Steenfelt A. and Simonetti A. (2011) Craton formation in Late Archean subduction zone revealed by first Greenland eclogites. *Geology* **39**, 1103–1106.

Taylor L. A. and Neal C. R. (1989) Eclogites with oceanic crustal and mantle signatures from the Bellsbank kimberlite, South Africa. Part I: mineralogy, petrography and whole rock chemistry. *J. Geol.* **97**(5), 551–567.

Taylor L. A., Snyder G. A., Keller R., Remley D. A., Anand M., Wiesli R., Valley J. W. and Sobolev N. V. (2003) Petrogenesis of group A eclogites and websterites: evidence from the Obnazhennaya kimberlite, Yakutia. *Contrib. Miner. Petrol.* **145**, 424–443.

Usui T., Nakamura E. and Helmstaedt H. (2006) Petrology and geochemistry of eclogite xenoliths from Colorado plateau: implications for the evolution of subducted oceanic crust. *J. Petrol.* **47**, 929–946.

van Westrenen W., Blundy J. D. and Wood B. J. (1999) Crystal-chemical controls on trace element partitioning between garnet and anhydrous silicate melt. *Am. Mineral.* **84**, 838–847.

van Westrenen W., Blundy J. D. and Wood B. J. (2001) High field strength element/rare earth element fractionation during partial melting in the presence of garnet: implications for identification of mantle heterogeneities. *Geochem., Geophys., Geosyst.* **2**, 2000GC000133.

Viljoen K.S., Robinson D.N., Swash P.M., Griffin W.L., Otter M. L., Ryan C.G., and Win T.T., 1994. Diamond - and graphite bearing peridotite xenoliths from the Roberts Victor kimberlite, South Africa. In: Meyer, H.O.A., Leonardos, O.H. (Eds.), Kimberlites, Related Rocks and Mantle Xenoliths. Proceedings of the Fifth International Kimberlite Conference. Companhia de Pesquisa de Recursos Minerais Special Publication 1B Jan/94, Araxa, Brasil, pp. 285–303.

Wang H., van Hunen J. and Pearson D. G. (in press) Making Archean cratonic roots by lateral compression: a two-stage thickening and stabilization model. *Tectonophysics*. http://dx.doi.org/10.1016/j.tecto.2016.12.001 (in press online).

Watson E. B. and Harrison T. N. (1983) Zirocn saturation revisited: temperature and composition effects in a variety of crustal magma types. *Earth Planet. Sci. Lett.* **64**, 295–304.

Wayte R. J., Worden R. H., Rubie D. C. and Droop G. T. R. (1989) A TEM study of disequilibrium plagioclase breakdown at high pressure: the role of infiltrating fluid. *Contrib. Miner. Petrol.* **101**, 426–437.

Wilkens R. H., Fryer G. J. and Karsten J. (1991) Evolution of porosity and seismic structure of upper oceanic crust: importance of aspect ratios. *J. Geophys. Res.* **96**(Bll), 17981–17995.

Wieczorek A., Libowitzky E. and Beran A. (2004) A model for the OH defect incorporation in kyanite based on polarized IR spectroscopic investigations. *Schweiz. Mineral. Petrograph. Mitt.* **84**, 333–343.

Zinngrebe, E., Foley, S.F., Vannucci, R., Bottazzi, P., Mattey, D. P., 1995. Metasomatism of peridotite by alkaline melt and cognate fluid: microchemical and ion probe evidence from the low-P Inagli dunite. In: 6th International Kimberlite Conference, Extended Abstracts, Novosibirsk, pp. 700–702.

Associate editor: Dmitri A. Ionov